Characterization and evaluation of submicron femtosecond laser-induced periodic surface structures on titanium to improve osseointegration of dental and orthopaedic implants

by

Hourieh Exir

Thesis submitted to the
Faculty of Graduate and Postdoctoral Studies
In partial fulfillment of the requirements
For the Master of Science in Physics

Ottawa-Carleton Institute of Physics
Department of Physics
University of Ottawa

Abstract

Surface properties such as topography and wettability play a pivotal role in controlling the cellular behavior on dental and orthopaedic implants and eventually their clinical success. The implementation of more advanced cell-targeted surface modification approaches has opened up additional possibilities for improving osseointegration to further increase the success rate of bone implants.

In this thesis, the potential of employing femtosecond laser-induced periodic surface structures with submicron spatial periodicities of 300 nm, 600 nm and 760 nm on titanium to improve osseointegration of dental and orthopaedic implants was explored. Uniform submicron femtosecond laser-induced periodic surface structures with consistent periodicity, roughness and oxide thickness were generated over large areas (10 x 10 mm^2) on titanium substrates and characterized using scanning electron microscopy (SEM), atomic force microscopy (AFM), electron energy loss spectroscopy (EELS), and Auger electron microscopy (AES). In vitro experiments using osteosarcoma Saos-2 cells showed the same level of cell metabolism on the laser textured and unmodified (control) surfaces along with statistically significant alkaline phosphatase activity after 14 days of cell seeding for the laser patterned surface with periodicity of 620 nm compared to the control surface. Average circularity along with nuclear area factor of cells fixed onto the laser textured and unmodified titanium surfaces were acquired from SEM images using ImageJ. The lower circularity and higher nuclear area factor of cells was observed on all laser textured surfaces as compared to the control, and are indicative of healthier cells on the laser textured surfaces. The cells appeared to align perpendicularly to the periodic laser generated structures and showed a more elongated shape on laser patterned surfaces as compared with the control surface, with the cell's filopodia appearing to be attached to the peaks of the laser-textured pattern.

In the second part of the thesis, the mechanism underlying the wettability transition from superhydrophilic to superhydrophobic on femtosecond laser generated periodic surface structures on titanium was investigated. The time-dependent wettability of the laser treated surfaces was assessed by the sessile drop method. The samples exhibited superhydrophilic behavior immediately after laser texturing and became superhydrophobic over time. Detailed

surface chemical analyses by X-ray photoelectron spectroscopy revealed that the unique electronic structures of Ti_2O_3 and TiO_2, which resulted in hydrophilic and hydrophobic hydration structures, respectively, played a crucial role in the observed wettability transition. This study demonstrates the prospect of using femtosecond laser-induced periodic surface structures as a promising surface modification strategy to potentially manipulate cellular behavior and improve dental and orthopaedic implants' clinical success rate.

Résumé

Les propriétés de surface telles que la topographie et l'humidejouent jouent un rôle central dans le contrôle du comportement cellulaire sur les implants dentaires et orthopédiques et, éventuellement, leur succès clinique. La mise en œuvre d'approches plus avancées de modification de surface ciblées sur les cellules a ouvert des possibilités supplémentaires d'amélioration de l'ostéointégration afin d'augmenter encore le taux de réussite des implants osseux.

Dans cette thèse, le potentiel d'employer des structures périodiques de surface induites par laser femtoseconde avec des périodicités spatiales submicron de 300 nm, 600 nm et 760 nm sur le titane pour améliorer l'ostéointégration des implants dentaires et orthopédiques a été exploré. Des structures périodiques périodiques induites par le laser sous-micron uniforme avec une périodicité, une rugosité et une épaisseur d'oxyde constantes ont été générées sur de grandes surfaces (10 x 10 mm^2) sur des substrats de titane et caractérisées à l'aide de la microscopie électronique à balayage (SEM)), la microscopie par force atomique (AFM), la spectroscopie de perte d'énergie électronique (EELS) et la microscopie électronique Auger (AES). Les expériences in vitro utilisant des cellules ostéosarcome Saos-2 ont montré le même niveau de métabolisme cellulaire sur les surfaces texturées et non modifiées (contrôle) au laser ainsi que l'activité de phosphatase alcaline statistiquement significative après 14 jours d'ensemencement cellulaire pour le laser surface modelée avec une périodicité de 620 nm par rapport à la surface de contrôle. La circularité moyenne ainsi que le facteur de surface nucléaire des cellules fixées sur les surfaces de titane texturées et non modifiées au laser ont été acquises à partir d'images SEM à l'aide d'ImageJ. La circularité inférieure et le facteur plus élevé de zone nucléaire des cellules ont été observés sur toutes les surfaces texturées de laser par rapport au contrôle, et sont indicatifs des cellules plus saines sur les surfaces texturées de laser. Les cellules ont semblé s'aligner perpendiculairement aux structures périodiques générées par laser et ont montré une forme plus allongée sur des surfaces à motifs laser par rapport à la surface de commande, avec la filopodia de la cellule semblant être attachée aux crêtes de la motif texturé au laser.

Dans la deuxième partie de la thèse, le mécanisme sous-jacent à la transition de la wettability de superhydrophile à superhydrophobe sur les structures périodiques de surface

générées par laser femtoseconde sur le titane a été étudié. La mouillabilité dépendante du temps des surfaces traitées au laser a été évaluée par la méthode de chute sessile. Les échantillons ont montré le comportement superhydrophilic immédiatement après texturation de laser et sont devenus superhydrophobes au fil du temps. Des analyses chimiques de surface détaillées par spectroscopie photoélectronique à rayons X ont révélé que les structures électroniques uniques de Ti_2O_3 et TiO_2, qui ont abouti à des structures d'hydratation hydrophiles et hydrophobes, respectivement, ont joué un rôle crucial dans l'étude transition humide. Cette étude démontre la perspective d'utiliser des structures périodiques de surface induites par le laser femtoseconde comme stratégie prometteuse de modification de surface pour manipuler potentiellement le comportement cellulaire et améliorer le taux de réussite clinique des implants dentaires et orthopédiques.

Acknowledgements

Foremost, I would like to thank my supervisor professor Arnaud Weck for believing in my abilities and giving me the liberty to pursue my ideas for my Master's studies. I am grateful to professor Weck, for his guidance during my graduate studies.

I would like to thank our collaborators, Mr. Bryan Lee and Dr. Kathryn Grandfield from McMaster University, for demonstrating the prospect of using submicron femtosecond laser-induced periodic surface structures on titanium to improve osseointegration of dental and orthopaedic implants.

I would like to acknowledge Dr. Alexander Mommers and Dr. Yun Liu at the Center for Catalysis Research and Innovation (CCRI), University of Ottawa, for their assistance with measurement of raw XPS data and SEM imaging and Dr. Xudong Cao for allowing me to perform the water contact measurements in the Chemical Engineering Department, University of Ottawa. I would also like to thank Mr. Anthony Olivieri at the Centre for research in photonics (CRPu), University of Ottawa, for the AFM training. I would also like to thank my colleagues at Fracture and Femtosecond Research Ottawa Group (FROG) lab of professor Weck, for their help with the trouble shooting of devices in the lab.

I wish to thank my family, for their continuous support and encouragement throughout my Master's studies.

List of publications

The work in this thesis is based on two manuscripts published in peer-reviewed journals.

1. Bryan E.J. Lee, Hourieh Exir , Arnaud Weck and Kathryn Grandfield
   Characterization and evaluation of femtosecond laser-induced sub-micron periodic structures generated on titanium to improve osseointegration of implants
   App. Surf. Sci. 441 (2018) 1034–1042.

2. Hourieh Exir and Arnaud Weck
   Mechanism of Superhydrophilic to Superhydrophobic Transition of Femtosecond Laser-Induced Periodic Surface Structure on Titanium
   Surf. Coat. Tech. 378 (2019) 124931.

Contents

Abstract ii

Résumé iv

Acknowledgements vi

List of publications vii

List of Abbreviations x

List of Figures xi

Chapter 1 1

Introduction 1

1.1 Overview 1
1.2 Contribution to the Field 2
1.3 Organization of the Thesis 3

Chapter 2 4

Literature Review 4

2.1 Factors Influencing the Success of Orthopaedic and Dental Implants 4
2.1.1 Biocompatibility 4
2.1.2 Osseointegration 4
2.1.3 Inherent Material Properties of Implants: Titanium 5
2.2 Modifications of Implant Surfaces 5
2.2.1 Grit-blasting 6
2.2.2 Acid-Etching 6
2.2.3 Plasma spraying 7
2.2.4 Anodization 8
2.3 Future of Implant Surface Modification 9
2.4 Surface Structuring with Femtosecond Laser 9
2.4.1 Mechanisms of Femtosecond Laser-Matter Interaction 10
2.4.2 Laser Ablation 10
2.4.3 Laser Induced Periodic Surface Structures 12
2.4.4 Femtosecond Laser Direct Writing Technique 13
2.5 Surface Wettability 15
2.5.1 Wetting on Ideal Flat Surface (Young's Model) 16
2.5.2 Wetting Theories of Rough Surfaces 17
2.5.2.1 Wenzel's Theory 17
2.5.2.2 Cassie-Baxter Theory 17

Chapter 3 18

Characterization and evaluation of femtosecond laser-induced sub-micron periodic structures generated on titanium to improve osseointegration of implants (Publication 1) 18

3.1 Author contribution: 18

Chapter 4 28

Mechanism of Superhydrophilic to Superhydrophobic Transition of Femtosecond Laser-Induced Periodic Surface Structure on Titanium **28**

(Publication 2) **28**

Hourieh Exir, and Arnaud Weck, "Mechanism of Superhydrophilic to Superhydrophobic Transition of Femtosecond Laser-Induced Periodic Surface Structure on Titanium", ... **28**

Surf. Coat. Tech. 378 (2019) 124931. ..... **28**

4.1 Author contribution: 28

Chapter 5 ..... **50**

Conclusions and Suggestions for Future Work **50**

Bibliography **52**

List of Abbreviations

AES	Auger Electron Spectroscopy
AFM	Atomic Forces Microscope
BIC	Bone-to-Implant Contact
CB	Cassie-Baxter
CCD	Charged Coupled Device
CAGR	Compound Annual Growth Rate
CA	Contact Angle
EELS	Electron Energy Loss Spectroscopy
Fs	femtosecond
FLIPSS	fs Laser-Induced Periodic Surface Structures
HSFL	High Spatial Frequency LIPSS
hMSCs	human mesenchymal stem cells
LIPSS	Laser-Induced Periodic Surface Structures
LSFL	Low Spatial Frequency LIPSS
ps	picoseconds
SEM	Scanning Electron Microscope
SP	Surface Plasmon
Ti	Titanium
TTM	Two-Temperature Model

List of Figures

Figure 2.1: SEM micrographs of Ti implant grit-blasted with (a) 25 um alumina particles and (b) 75 μm alumina particles. Arrow shows the particle contamination [28]. The scale bar is 10 μm. 6

Figure 2.2: SEM micrograph of an acid-etched Ti implant. The scale bar is 6 um [32]. 7

Figure 2.3: SEM micrographs of a Ti plasma sprayed implant surface [8]. The scale bar for image (a) is 100 μm and for image (b) is 10 μm. 8

Figure 2.4: The top and cross-section SEM images of titania nanotubes produced in 1 M H_3PO_4 + 0.3 wt% HF at (a) 10 V and (b) 20 V for 1 h [34]. 8

Figure 2.5: Schematic layout of a typical for direct fs laser surface writing consisting of fs laser, half-wave plate (HWP), glan polarizer (GP), shutter (SH), mirrors (M1 and M2), dichroic mirrors (DM1 and DM2), charged coupled device (CCD), objective lens (OL) computer controlled XY-translation stage..... 14

Figure 2.6: Schematics of the laser pulse overlapping to create lines and areas on a substrate. 15

Figure 2.7: Wetting behavior of a liquid droplet on an ideal solid surface (Young's state) where θ_γ is the equilibrium contact angle, γ_{SA} is the solid-air interfacial tension, γ_{SL} is the solid-liquid interfacial tension and γ_{LA} is the liquid-air interfacial tension on the solid [69]. 16

Chapter 1

Introduction

1.1 Overview

Orthopedic and dental implants are used to replace or support missing or damaged bone, joint or tooth due to accidents, disease or aging [1]. All medical implants are made of materials, known as biomaterials, defined as "a substance that has been engineered to take a form which, alone or as part of a complex system, is used to direct, by control of interactions with components of living systems, the course of any therapeutic or diagnostic procedure, in human or veterinary medicine" [2]. Over the last 4 decades, progress in medical technology and biomaterials has paved the way to creating innovative biomaterials to improve the quality of life and longevity of patients [3]. The field of orthopaedic and dental implants is rapidly growing to keep with the demands of an aging population and also younger patients. According to the latest market research report, global orthopedic implants market is projected to expand from USD $52.8 billion in 2017 to USD $66.2 billion in 2023 at a steady compound annual growth rate (CAGR) of 3.8% [4] and the global dental implants market is projected to grow from USD $3.60 billion in 2016 to USD $6.54 in 2025 at CAGR of 6.9% [5]. Orthopedic and dental implants suffer from their limited lifetime of 10 to 15 years inside the body caused by corrosion, high modulus of elasticity of implant relative to that of bone, infection and lack of osseointegartion (i.e., a direct structural and functional connection between ordered, living bone and the surface of a load-carrying implant) [6]. The major causes of implant failures are attributed to lack of osseointegration and infection, leading to revision surgeries, which are more challenging, expensive and have small success rate [3]. Thus, much room remains for the improvements of implants with better biocompatibility and higher lifespan to reduce the occurrence of failure.

Based on earlier research findings that cells can recognize nano and micron features on the surface and respond by changing their morphology and behavior, the bone-implant material development has shifted from basic a bioinert (i.e., inertness with living tissue or no release of toxic substances) concept towards more complex cell-targeted surface

modification approaches that mimic extracellular microenvironment to control cellular behavior like attachment, migration, spreading, proliferation and differentiation to induce controlled, guided, and rapid healing and improve the implant's performance and longevity solely by tuning the biomaterial's physiochemical and topographical surface properties [6, 7]. The commercially successful implant surface treatments for dental and orthopedic implants such as acid etching, sandblasting and anodization contaminate the surface and create stochastic features on implant surface [8, 9]. During the last decade, femtosecond (fs) laser surface structuring has emerged as a simple, high resolution, fast, controllable, reproducible, contactless, single step processing technique applicable to a wide class of materials, including metals [10], semiconductors [11, 12], and polymers [13], by generating spatially periodic structures known as laser-induced periodic surface structures (LIPSS) or ripples. The formation of the periodic ripples with spatial periods close to the wavelength of the laser was attributed to the interference between the incident laser beam and the surface scattering wave [14]. Recently, a revised scattering model was proposed [15] explaining the formation of ripples in terms of the initial direct surface plasmon (SP)-laser interference and the subsequent grating-assisted SP-laser coupling. High biocompatibility, corrosion resistance, and strength to weight ratio have led Titanium (Ti) to be successfully used in many biomedical, aeronautical, and industrial applications [16].

1.2 Contribution to the Field

The principal goal of this thesis was to evaluate the potential of fs LIPSS with submicron spatial periodicities of 300 nm, 600 nm and 760 nm on grade 2 Ti (99%, ultra-corrosion-resistant) to improve osseointegration of dental and orthopedic implants. In addition, numerous studies have demonstrated the critical role the surface wettability of the implants plays in regulating the important physiological processes such as protein adsorption, cell adhesion, and cell proliferation [17]. Therefore, in the second part of the present thesis, the mechanism underlying the wetting transition of fs laser generated LIPSS on grade 2 Ti was systematically assessed by analyzing the surface chemical compositions of different aged surfaces: the fresh laser textured surface, and laser textured surfaces aged under ambient conditions for 45 days and a year.

1.3 Organization of the Thesis

In chapter 1, an overview on the field of orthopaedic and dental implants along with the recent innovative directions to improve the implant's performance and longevity are presented.

Chapter 2 provides a detailed literature review on the principal factors determining the success of orthopedic and dental implants, major implant surface modification methods in use today along with the future ones, femtosecond laser direct writing technique and the surface wettability.

In chapter 3, generation and surface characterizations of submicron femtosecond laser-induced periodic surface structures (FLIPSS) with consistent periodicities of 300 nm, 620 nm and 760 nm on titanium covering the entire sample with no other features appearing (e.g., due to the line spacing) along with *in vitro* bioactivity assessments of oasteosarcoma Saos-2 cells on the FLIPSS are presented.

In chapter 4, the mechanism underlying the gradual evolution of surface wettability of FLIPSS over time from superhydrophilicity to superhydrophobicity through detailed XPS study was revealed.

Chapter 5 provides a summary of the major findings along with suggestions for future work.

Chapter 2

Literature Review

2.1 Factors Influencing the Success of Orthopaedic and Dental Implants

2.1.1 Biocompatibility

Biocompatibility is defined as “the ability of a material to perform with an appropriate host response in a specific application” [18]. That means the implants should possess high level of nontoxicity and the materials or any leachable products from it must not trigger cell death or any inflammatory or allergic reactions in the body [3]. The concept of biocompatibility comprises both compatibility of the material with the tissue (biological compatibility) and its ability to perform specific function. The main factors affecting the biocompatibility are chemical composition, mechanical properties and surface features [19].

2.1.2 Osseointegration

In 1952, Per-Ingvar Brånemark and his team were conducting research on blood flow in the bone-healing process by inserting Ti optic chambers into the lower leg bones of rabbits. At the conclusion of the experiment, when it became time to remove the microscope heads from the bone, he discovered that the bone had firmly integrated with the titanium and was difficult to remove. Brånemark called "the direct structural and functional connection between ordered, living bone and the surface of the load-carrying implant, without intervening soft tissue” osseointegration [20]. The degree of integration of the implant with the surrounding bone decides the outcome of the implant surgery. The higher the degree of osseointegartion establishes a higher mechanical stability and lowers the probability of implant loosening and failure. Adhesion of the cells to the surface of implant and reduction of micromotion is critical for a successful osseointegration and is highly influenced by the physiochemical properties and nanometer and micrometer scale topographies [3].

2.1.3 Inherent Material Properties of Implants: Titanium

Titanium is the preferred material for orthopedics and dental implants due to combination of desirable characteristics including formation of a very stable surface oxide layer of titania on its surface of thickness between 5-10 nm immediately after exposure to air that provides Ti with superior biocompatibility and high corrosion resistance [19]. The low elastic modulus of Ti (105 GPa) is crucial for hard tissue replacement to ensure smaller stress shielding, a phenomenon where due to the dissimilarity of modulus of elasticity of implant and bone, reabsorption of bone and implant loosening occurs, leading to revision surgery [3].

2.2 Modifications of Implant Surfaces

The significance of implant surface topography for successful osseointegration was first indicated by Albrektsson et al. in 1981 [21]. Since then, there have been many studies demonstrating the effect of surface roughness on the rate and extent of osseointegration of dental implants [8, 23]. Menezes et al. observed that osteoblast cells show an increase in cell attachment and proliferation on rougher Ti surfaces when compared with smooth ones *in vitro* [19]. The improved bone integration of implants with increased surface roughness was demonstrated *in vivo* by Grizon et al. [24]. Therefore, in recent years the primary goal of biomedical research efforts has been focused on surface modifications to create topographies on implant surfaces to optimize osteoblast cells migration, adhesion, proliferation, and differentiation. The implant surface roughness depending on the scale of the different surface features can be classified into macro-, micro- and nano scale [23]. The macro roughness is termed for topographical features ranging from millimeters to tens of microns and is determined by implant's visible geometry, such as threaded screw and tapered design. Previous studies have shown that the initial implant stability and long-term fixation are improved by mechanical interlocking between the implant macro rough surface and bone. The micro roughness is for features ranging from 1-10 microns. Micron level surface topography increases the bone-implant interface area and enhances growth and interlocking of bone at the implant interface [25]. The submicron roughness features ranges from 0.1-1 μm [26] and studies have shown greater osteoblast differentiation and maturation *in vitro* and osseointegration *in vivo* on implants with submicron textured roughness [27]. The nano

roughness features ranges from 1-100 nm and is considered to promote absorption of proteins and adhesion of osteoblasts resulting in enhanced osseointegration [25].

To increase the surface roughness of implants, the following major surface modification methods for implants are used.

2.2.1 Grit-blasting

In grit-blasting hard ceramic particles such as alumina, titania or hydroxyapatite particles are projected at high velocities using compressed air at implant surface to modify the implant surface. In a study done by Wennerberg et. al [28], implant surfaces were blasted with 25 μm or 75 μm alumina particles (Figure 2.1) and inserted in the rabbit tibia and femur and after 12 weeks, the rougher 75 um blasted surface showed a higher removal torque and more bone-to-implant contact (BIC) than the 25 um ones. In a human study, the titania blasted implant showed a higher BIC than in regular machined surfaces which was confirmed by other studies [29]. Other clinical studies reported a high success rate of up to ten years for the titania grit- blasted implants [30].

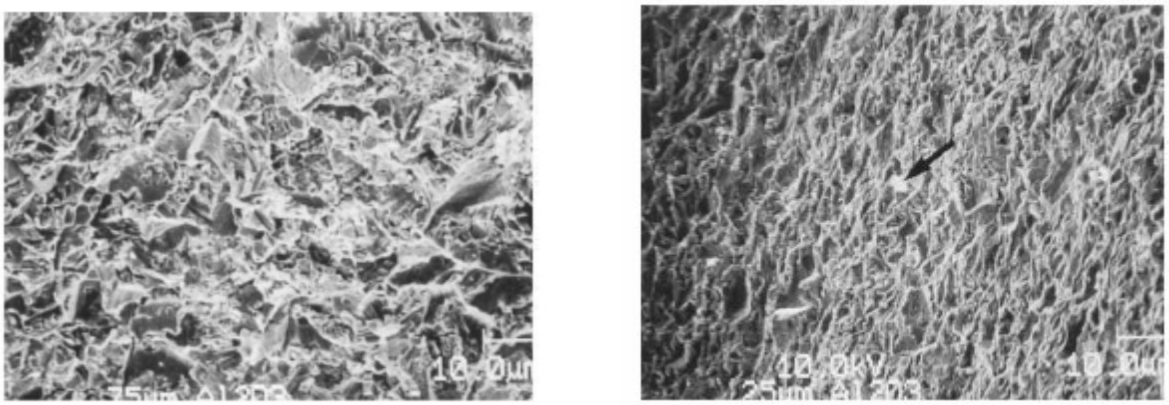

Figure 2.1: SEM micrographs of Ti implant grit-blasted with (a) 25 um alumina particles and (b) 75 μm alumina particles. Arrow shows the particle contamination [28]. The scale bar is 10 μm.

2.2.2 Acid-Etching

In surface modification by acid-etching, the Ti implant is immersed in strong acids such as H_2SO_4, HCl, HNO_3 and HF, eroding the surface to produce micro pits with sizes ranging

from 0.5 µm to 2 µm in diameter [8, 31]. An example of an acid-etched titanium surface is shown in Figure 2.2 [32]. Acid-etching surfaces exhibited favorable cell adhesion and thereby enhanced osseointegration. It is found that in dual-acid etched technique where a mixture of acids are used to produce a micro rough implant surface, adhesion of osteogenic cells, and thus bone formation directly on the surface of implant was promoted. The acid-etching causes hydrogen embrittlement of the titanium that creates micro cracks on its surface and thus reduces the fatigue resistance of the implant leading to fracture [8, 31].

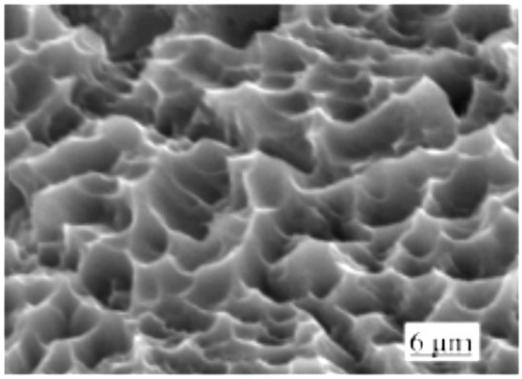

Figure 2.2: SEM micrograph of an acid-etched Ti implant. The scale bar is 6 um [32].

2.2.3 Plasma spraying

The other technique used in modification of implant surfaces is plasma spraying in which powders of Ti or calcium phosphates are heated to high temperatures and then blasted onto implant surfaces to form 30 µm to 50 µm thick coatings. An example of a Ti plasma sprayed surface is shown in Figure 2.3 [8]. It was shown in a pre-clinical study on minipigs that bone-implant interface formed faster with Ti plasma sprayed surface as compared with uncoated implants [8]. However, these coatings may be susceptible to delamination or resorption after long periods in use and can adversely affect the mechanical integrity causing periimplantitis (i.e., an infectious disease occurring in tissues around an osseointegrated implant resulting in loss of supporting bone) [31, 33].

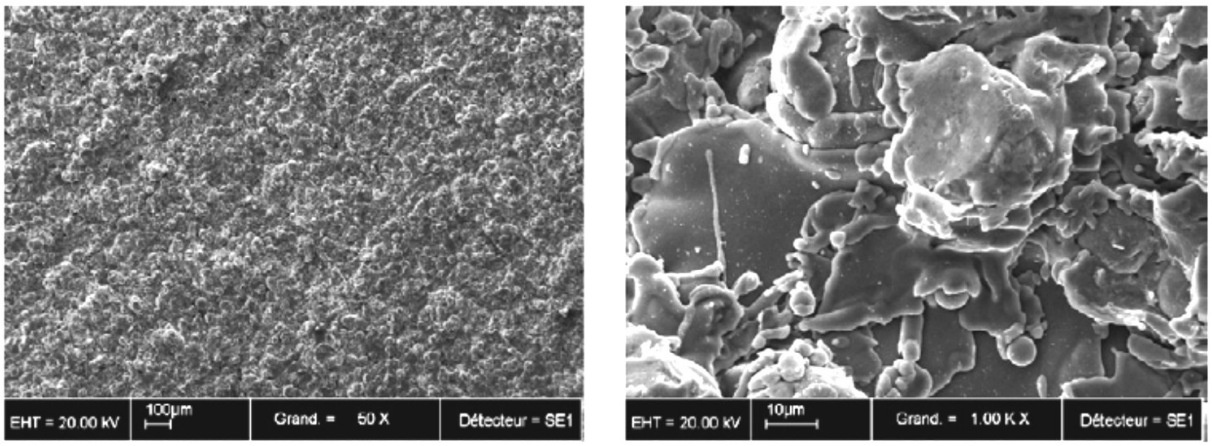

Figure 2.3: SEM micrographs of a Ti plasma sprayed implant surface [8]. The scale bar for image (a) is 100 µm and for image (b) is 10 µm.

2.2.4 Anodization

In anodization technique, the implant is placed as anode in an electrochemical cell to increase the oxide layer thickness and generate micro-or nano-pores with variable diameters. Anodized implants show increased cell attachment and proliferation [31]. The top and cross-section SEM images of titania nanotubes produced by anodization are shown in Figure 2.4 [34]. It was shown in a preclinical study in a rabbit model that the BIC was slightly higher in anodized Ti implants than on untreated one. In human clinical studies, increased BIC compared to untreated Ti was also reported [23].

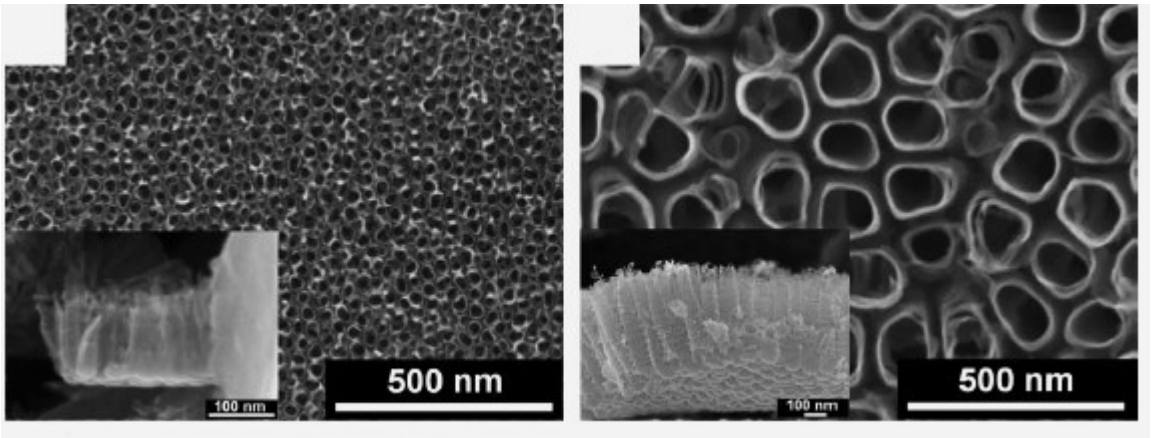

Figure 2.4: The top and cross-section SEM images of titania nanotubes produced in 1 M H_3PO_4 + 0.3 wt% HF at (a) 10 V and (b) 20 V for 1 h [34].

2.3 Future of Implant Surface Modification

Most of the surface modification techniques in use today show random surface topographies with features ranging from nanometers to millimeters. To gain insight into the influence of these topographical features on osteoblast cell behavior at the cellular level to improve osseointegtarion, surfaces with topography in nanoscale are required. To create modifications to the topography and chemistry of the surface in a reproducible manner, the most promising methods are lithography based that are borrowed from the semiconductor electronics industry [8]. However, they require expensive equipment, are time consuming and have small surface coverage [35]. For multiscale process like osseointegration, insight and control of surface properties over different scales are required. During the last decade, fs lasers have emerged as a simple, high resolution, fast, controllable, reproducible, contactless processing technique applicable to a wide class of materials [10-13], to machine micro- and nanoscales features in a single step over large area, making it a very promising surface modification technique for scaling it up to industrial production [36]. Several groups studied the effect of fs laser textured surfaces on the behavior of cells *in vitro*. Carvalho et al. [37] found that cell attachment, alignment, migration and proliferation were modulated preferentially by surface microtopography, and human mesenchymal stem cells (hMSCs) undergo a faster and higher osteogenic differentiation on these laser textured surfaces than on unstructured control surfaces Cunha et al. studied the spreading, adhesion, and differentiation of hMSCs on fs laser textured surfaces and observed the laser textured surface can trigger the stretching of hMSCs, and is potentially capable of improving osseointegration of titanium orthopedic and dental implants [38].

2.4 Surface Structuring with Femtosecond Laser

In recent years, fs laser surface structuring has emerged as a simple, high resolution, fast, controllable, reproducible, contactless processing technique applicable to a wide class of materials, including metals [10], semiconductors [11, 12], and polymers [13], to fabricate a variety of micro- and nanoscales features in one single step over large areas, making it a very promising surface modification technique for scaling it up to industrial production. Different micro- and nanostructures on the surface of the material can be formed by changing various

parameters, such as fluence, wavelength, number of pulses, scan velocity, laser polarization, incident angle, and environment [39]. With fs laser structuring it is possible to control the optical, mechanical, wetting, chemical and biological properties of a solid surface and to fabricate novel materials for a wide range of applications in photonics, plasmonics, micro/nanofluidics, wetting and biomedical applications [40].

2.4.1 Mechanisms of Femtosecond Laser-Matter Interaction

The fs laser-matter interaction processes take place over a short duration of time leading to ablation and the formation of surface structures. After a metal surface is exposed to a fs laser pulse, the pulse energy is absorbed by the electrons, the electrons are excited on a time scale of 100 fs and thermalization of the energetic electrons (hot electrons) takes place in a few tens of fs, leading to an electron temperature much higher than the lattice temperature while the lattice temperature remains at the initial room temperature. Therefore, the system is out of thermal equilibrium consisting of two subsystems, the hot electrons and cold lattice. The two-temperature model (TTM) is used to describe the temperature dynamics for this nonequilibrium system. The hot electrons are cooled down by hot electron diffusion and electron-phonon interactions establishing the thermal equilibrium in the system between lattice and electrons within a few picoseconds (ps). For sufficiently elevated lattice temperature, surface melts on a timescale between a few and a hundred ps and surface ablation occurs within a few tens of ps after the laser pulse strikes the surface of the material and carries on up to several nanoseconds (ns). Then, the ablated material rapidly cools down and resolidifies leading to the formation of self-organized patterns frozen on the surface, and some of the generated nanoparticles during ablation are redeposited to further change the morphology of the surface [39, 41].

2.4.2 Laser Ablation

Laser-mater interaction leads to laser ablation which is defined as removal of material from the surface under laser irradiation occurring above the ablation threshold that eventually leads to the formation of micro- and nanoscales structures. The ablation threshold is the minimum amount of energy required to initiate the material removal process. The mechanism of laser-matter interaction and ablation depends on the material properties and

the laser parameters such as fluence (i.e., ratio of laser pulse energy (J) to the irradiated area (cm^2)) wavelength and pulse duration [39].

For a Gaussian beam distribution, the spatial fluence profile, in a plane perpendicular to the laser beam $\phi(r)$, is defined as:

$$\phi(r) = \phi_0 \, e^{-2r^2/\omega_0^2} \tag{1}$$

where r is the distance from the center of the beam, and ω_0 is the laser beam radius at e^{-2} of the maximum intensity. The peak fluence (ϕ_0) is related to the laser pulse energy (E_p) according to:

$$\phi_0 = \frac{2E_p}{\pi {\omega_0}^2} \tag{2}$$

The laser pulse energy (E_p) is given by:

$$E_p = \frac{p_{av}}{f} \tag{3}$$

where p_{av} (W) is the average power of the laser beam measured with a power meter and f (Hz) is the repetition rate of the laser. It has been shown that for a Gaussian beam with radius ω_0, the diameter of an ablated crater D is related to the peak laser fluence (ϕ_0) according to:

$$D^2 = 2\omega_0^2 ln\left(\frac{\phi_0}{\phi_{th}}\right) \tag{4}$$

where (ϕ_{th}) is the ablation threshold fluence of the material. On account of the linear dependence of the peak laser fluence (ϕ_0) on the pulse energy, the Gaussian beam radius (ω_0) is obtained from a linear plot of the squares of the average ablated crater diameter (D^2) versus the logarithm of the laser pulse energy, $ln(E_p)$. From the slope m of the linear fit to the (semi-logarithmic plot of D^2 versus the $ln(E_p)$, the beam radius is found according to:

$$\omega_0 = \sqrt{\frac{m}{2}} \tag{5}$$

With this technique the Gaussian beam radius at the interaction surface is determined [39, 42, 43].

2.4.3 Laser Induced Periodic Surface Structures

In 1965, Birnbaum was the first to observe a series of parallel periodic surface grating patterns, a phenomenon known as LIPSS on semiconductor surfaces irradiated with a ruby laser [44]. In recent years, fs laser has emerged as a simple technique to fabricate fs LIPSS (FLIPSS) on a variety of materials, including semiconductors [45-48], metals [49-52], polymers [13] and dielectrics [53-55] to tailor the optical, mechanical, and chemical properties of the surfaces to eventually fabricate novel materials for a wide range of applications in photonics, micro/nanofluidics, wettability, tribology and biomedical applications [40, 56, 57]. FLIPSS can be classified as Low Spatial Frequency LIPSS (LSFL), with periods on the order of the incident laser wavelength and oriented perpendicularly to the incident laser beam polarization, and High Spatial Frequency LIPSS (HSFL), having periods much smaller than the laser wavelength and with an orientation either parallel or perpendicular to the incident polarization [58]. It has been shown by previous studies that the spatial period of LIPSS can be controlled by wavelength [51, 59], angle of incidence [60] and refractive index [51] while its orientation depends on polarization of incident laser beam [61, 62]. Recent studies have revealed the orientation of the LIPSS can be modified by varying states of laser polarization (linear, circular or elliptical). When linearly polarized laser beam is applied, the ripples are aligned either perpendicular or parallel to the incident laser polarization [63]. Wang et al. [63] reported that under the irradiation of left and right circularly polarized fs laser pulses the ripples were angled at +45° and −45° with respect to the incident plane of the beam, respectively. On the contrary, the elliptically polarized fs laser pulses induced ripples that were aligned perpendicular to the long axis, as demonstrated by Tang et al. [64] and Varlamova et al. [65]. The formation of the periodic ripples with spatial periods close to the wavelength of the laser was attributed to the interference between the incident laser beam and the surface scattering wave that was developed by Sipe and co-workers [14]. Recently, Huang et al. [15] proposed a revised scattering model explaining the formation of ripples in terms of the initial direct SP-laser interference and the subsequent grating-assisted SP-laser coupling. The key underlying reasons behind decreasing of the spatial period of the ripples as number of laser pulses increases is discussed as a mixture of field-distribution effect and grating-coupling effects. As observed, for the Gaussian distribution of laser beam, the spatial period of the ripples depends on the laser intensity.

With increasing pulse number, the diameter of the laser ablated crater increases and the spatial period of the ripples decreases. As moving away from the center towards the perimeter of the laser ablated crater, the laser intensity decreases leading to lowering of electron density at the laser ablated crater periphery causing the wavelength of the surface plasmon polaritons to shorten, decreasing the spatial period of the ripples. In addition, the groove depth also has important effects on the ripples spatial periodicity. As the number of pulses increase, the ripples deepen, and the wavelength of the surface plasmon polaritons will decrease. The laser fields are more localized in the grooves and absorbed more efficiently, leading to a strong positive feedback and the grating-assisted SP-laser coupling efficiency is enhanced. The enhanced laser field enhancement allowing for more efficient laser fields coupled to the SPs; result in smaller ripple spatial period. However, the high fluence in the center of the laser ablated crater causes a strong thermal effect, creating a thick melted layer which weakens the grating-coupling effect and ripples with periodicity near laser wavelength with interference mechanism are created [15].

2.4.4 Femtosecond Laser Direct Writing Technique

A typical setup for fs laser direct writing is shown in Figure 5. A variety of micro- and nanoscales features in one single step on a wide class of materials can be fabricated in a reproducible manner with the laser direct writing technique depending on the laser beam and processing parameters. The fs laser beam is passed through a series of optical elements to finally impinge on the surface of the sample. The combination of a Glan polarizer and a half wave plate is employed to vary the laser power. A shutter is used to control the number of pulses from a fs laser impinging on a stationary sample. For the non-stationary case in direct fs laser writing, the sample is translated with respect to the stationary laser beam to generate a line or an area on the surface of the sample where the number of laser pulses per shot is also controlled by varying the scan velocity. Afterwards, a series of mirrors (M1, M2, and dichroic mirror (DM) are used to direct the laser beam into an objective lens (OL). The sample is mounted on a computer-controlled XY-translation stage and illuminated from the top to enable monitoring of the laser micromachining processes with a CCD camera. The fs laser micromachining setup shown in Figure 2.5 can be used for ablating a spot on the sample when the translation stage is stationary, generating a single line when the sample is

translating along the X- or Y- axis by overlapping successive laser pulses in the scanning direction or by allowing a certain amount of overlapping between successive scanned lines, termed line overlap, to achieve surface coverage of an area [39, 40].

The pulse overlap (φ_{pulse}) is the percentage amount of overlap between successive laser pulses and can be varied by the scanning speed v and pulse repetition rate f. The line overlap (φ_{line}) is controlled by setting line spacing Δx, which represents the distance between the centers of the two successive laser scanned tracks [39]. The schematic representation of the pulse and line overlaps is shown in Figure 2.6.

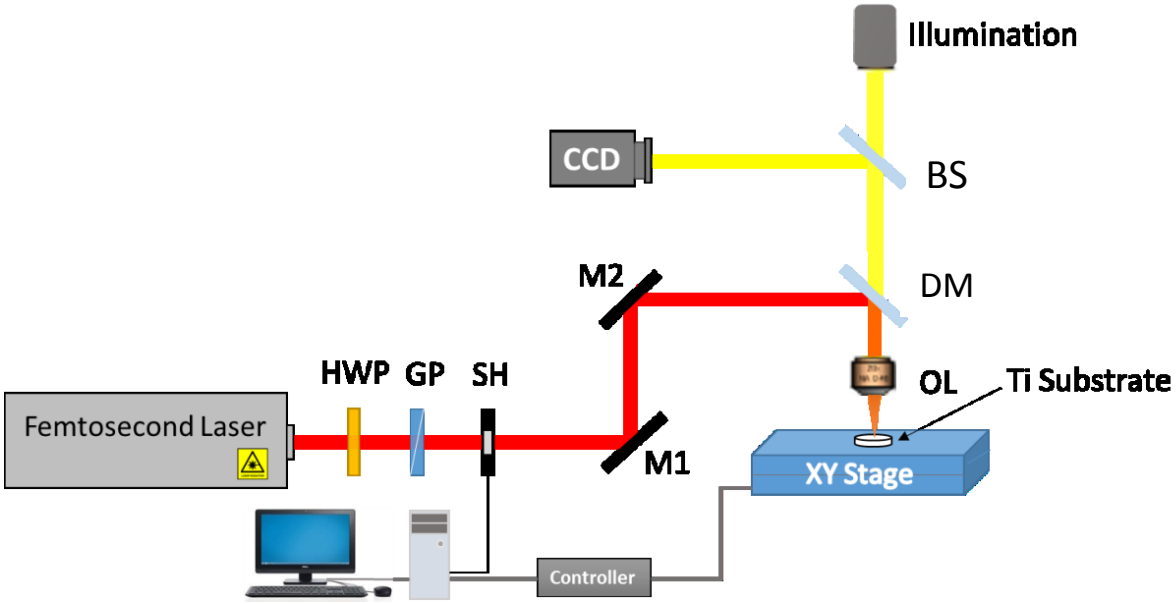

Figure 2.5: Schematic layout of a typical for direct fs laser surface writing consisting of fs laser, half-wave plate (HWP), Glan polarizer (GP), shutter (SH), mirrors (M1 and M2), dichroic mirror (DM), beam splitter (BS), charged coupled device (CCD), objective lens (OL) computer controlled XY-translation stage.

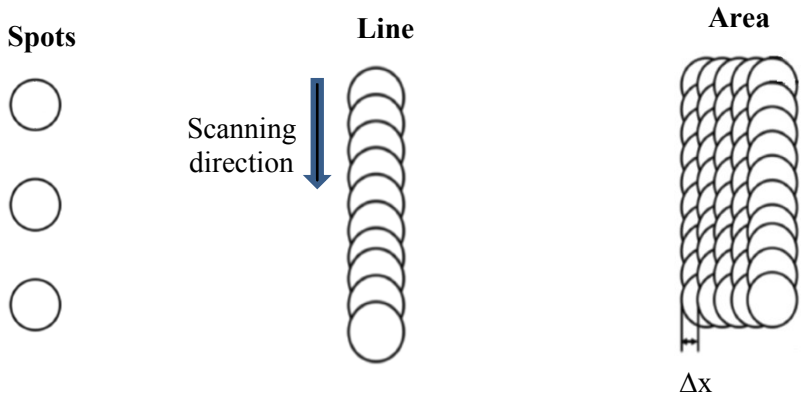

Figure 2.6: Schematics of the laser pulse overlapping to create lines and areas on a substrate.

Percentage of pulse and line overlaps are given by,

$$\varphi_{pulse} = \left(1 - \frac{\upsilon}{fD}\right) \times 100 \tag{6}$$

$$\varphi_{line} = \left(1 - \frac{\Delta x}{D}\right) \times 100 \tag{7}$$

where υ is the scanning speed, f is the repetition rate, D is the laser spot diameter, and Δx is the line spacing [39].

2.5 Surface Wettability

The surface wettability, which is the degree to which a liquid spread over a solid, is an important property of a solid surface. For decades, modifying and controlling the surface wettability of biomaterials have been the focus of extensive research. Numerous studies have demonstrated the critical role the surface wettability of the biomaterials plays in regulating the important physiological processes such as protein adsorption, cell adhesion, and cell proliferation [66, 67].

2.5.1 Wetting on Ideal Flat Surface (Young's Model)

The main method to quantitatively measure the surface wettability is by measuring the contact angle (CA) of a liquid droplet on a surface, which is the angle between the solid-liquid interface and the tangent of the liquid-air interface at the three phases boundary [68], as shown in Figure 7 [69]. The CA of a liquid on an ideal solid surface that is flat and chemically homogeneous can be described through balancing the interfacial tensions between a solid and air (γ_{SA}), liquid and solid (γ_{SL}), liquid and air (γ_{LA}) on the solid, obtaining Young's equation [69, 70] ,

$$\cos\theta_Y = \frac{\gamma_{SA}-\gamma_{SL}}{\gamma_{LA}} \tag{6}$$

where θ_Y is the equilibrium contact angle, as illustrated in Figure 2.7. In principle, surfaces with a water CA lower than 90^o are considered hydrophilic and those with water CAs between 90^o and 150^o are termed hydrophobic.

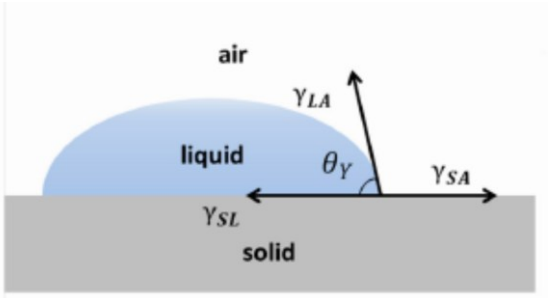

Figure 2.7: Wetting behavior of a liquid droplet on an ideal solid surface (Young's state) where θ_Y is the equilibrium contact angle, (γ_{SA}) is the solid-air interfacial tension, (γ_{SL}) is the solid-liquid interfacial tension and (γ_{LA}) is the liquid-air interfacial tension on the solid [69].

2.5.2 Wetting Theories of Rough Surfaces

In reality, all surfaces are not ideal and can have roughness and chemical heterogeneity; thereby two models, the Wenzel and the Cassie-Baxter (CB) were developed to describe the behavior of the liquid on the real surfaces [72].

2.5.2.1 Wenzel's Theory

In the Wenzel model, the liquid completely wets the grooves of a rough surface, creating a homogeneous solid/liquid interface. According to the Wenzel theory [72], the increase in surface roughness has an amplification effect on the wettability expressed as follows [73, 74],

$$\cos\theta^* = r\cos\theta_Y \tag{9}$$

where r is the roughness factor (r >1) defined as the ratio of the actual area to the flat projected area, θ^* and θ_Y are the apparent contact angle and the equilibrium contact angle from Young equation, respectively. Eq. (9) suggests that increasing the surface roughness amplifies the surface inherent wetting behavior, making the hydrophilic surfaces more hydrophilic and hydrophobic surfaces more hydrophobic.

2.5.2.2 Cassie-Baxter Theory

In the CB model, the liquid incompletely wets the rough surface, forming a solid/liquid-air composite interface. According to the CB theory [75], the contact angle of the liquid on this composite surface is expressed as [74],

$$\cos\theta^* = fr_f\cos\theta_Y + f - 1 \tag{10}$$

where θ^* is the apparent contact angle and θ_Y is the equilibrium contact angle on the solid with f and r_f being the fraction of wet solid underneath the water droplet and the roughness factor of the wetted area, respectively. The higher the area fraction of the air trapped underneath the droplet, the higher the contact angle.

Chapter 3

This chapter is based on the following published paper:

Characterization and evaluation of femtosecond laser-induced sub-micron periodic structures generated on titanium to improve osseointegration of implants (Publication 1)

Bryan E.J. Lee, Hourieh Exir, Arnaud Weck, and Kathryn Grandfield, "Characterization and evaluation of femtosecond laser-induced sub-micron periodic structures generated on titanium to improve osseointegration of implants", *App. Surf. Sci.* 441 (2018) 1034.

3.1 Author contribution:

H. Exir conceived the idea of this work. The experimental design and femtosecond laser micromachining of all the samples used in this study were performed by H. Exir at the Fracture and Femtosecond Research Ottawa Group (FROG) of professor Weck, in the Colonel By building (CBY), at University of Ottawa, under the supervision of professor Weck. All the microscopy work was carried out at the Canadian Centre for Electron Microscopy, McMaster University, by B. Lee. In vitro studies were designed and performed at the Biointerfaces Institute at McMaster University, by B. Lee. All the characterizations and detailed analysis of the data were conducted by B. Lee, under the supervision of Dr. Kathryn Grandfield. The manuscript was mainly written by B. Lee and in part by H. Exir. All authors contributed to the final manuscript.

Applied Surface Science 441 (2018) 1034–1042

Contents lists available at ScienceDirect

Applied Surface Science

journal homepage: www.elsevier.com/locate/apsusc

Full Length Article

Characterization and evaluation of femtosecond laser-induced sub-micron periodic structures generated on titanium to improve osseointegration of implants

Bryan E.J. Lee [a], Hourieh Exir [b,c], Arnaud Weck [b,c,d], Kathryn Grandfield [a,e,*]

[a] School of Biomedical Engineering, McMaster University, Hamilton, Canada
[b] Department of Physics, University of Ottawa, Ottawa, Canada
[c] Centre for Research in Photonics at the University of Ottawa, Ottawa, Canada
[d] Department of Mechanical Engineering, University of Ottawa, Ottawa, Canada
[e] Department of Materials Science and Engineering, McMaster University, Hamilton, Canada

ARTICLE INFO

Article history:
Received 6 November 2017
Revised 31 January 2018
Accepted 11 February 2018
Available online 13 February 2018

Keywords:
Titanium
Implant
Osseointegration
Periodicity
Femtosecond laser

ABSTRACT

Reproducible and controllable methods of modifying titanium surfaces for dental and orthopaedic applications are of interest to prevent poor implant outcomes by improving osseointegration. This study made use of a femtosecond laser to generate laser-induced periodic surface structures with periodicities of 300, 620 and 760 nm on titanium substrates. The reproducible rippled patterns showed consistent submicron scale roughness and relatively hydrophobic surfaces as measured by atomic force microscopy and contact angle, respectively. Transmission electron microscopy and Auger electron spectroscopy identified a thicker oxide layer on ablated surfaces compared to controls. *In vitro* testing was conducted using osteosarcoma Saos-2 cells. Cell metabolism on the laser-ablated surfaces was comparable to controls and alkaline phosphatase activity was notably increased at late time points for the 620 and 760 nm surfaces compared to controls. Cells showed a more elongated shape on laser-ablated surfaces compared to controls and showed perpendicular alignment to the periodic structures. This work has demonstrated the feasibility of generating submicron features on an implant material with the ability to influence cell response and improve implant outcomes.

1. Introduction

Various methods of modifying titanium have been examined to improve its suitability as an implant material. The goal of these modification techniques is to improve the overall osseointegration, otherwise known as a structural and functional connection, between native bone and the implant material, often achieved by modulating the surface chemistry and topography [1]. These changes often arise from the generation of roughened or porous surface features, which are known to stimulate cellular adhesion and promote bone growth by increasing the bone-implant interface surface area [2,3].

Laser machining, historically, has primarily been used in the semi-conductor industry but has gained traction in recent times as an unconventional implant modification technique [4–8]. Laser machining alters material properties by remelting, alloying or cladding substrate surfaces [7]. The main benefits of using laser-based modification techniques, compared to other surface modification techniques, are that they allow for a degree of precision and control over features while being non-contact, quick, and clean [9]. This degree of precision is a limitation to many other modification techniques such as acid-etching, particle deposition, electropolishing and electric discharge machining [10–14]. Surface geometries achieved via laser modification techniques have ranged from holes, to crown-like projections, to rippled patterns [7,15,16]. Many attempts to use laser modification as a machining technique tend to also result in the formation of holes, cracks and craters, both by design and as a result of thermal damage [6,8,17]. Laser texturing has been used in the biomedical field as a method of altering surface topography to potentially improve osseointegration. Studies involving laser ablation have shown that both osteoblast differentiation and mesenchymal stem cell differentiation towards osteogenic fates can both be increased when interfacing with laser-ablated surfaces [8,15,16,18,19]. In addition, relatively random laser induced microtopographies on conventional implants have

* Corresponding author at: Department of Materials Science and Engineering & School of Biomedical Engineering, McMaster University, Hamilton, Canada.
E-mail address: kgrandfield@mcmaster.ca (K. Grandfield).

https://doi.org/10.1016/j.apsusc.2018.02.119
0169-4332/

demonstrated improved osseointegration *in vivo* with these implanted materials [15,20–22].

Irradiation with linearly polarized ultrashort pulses, using a femtosecond laser, can generate laser-induced periodic surface structures (LIPSS), or ripples, on numerous types of materials, including common implant materials such as titanium [23], [24]. Recent studies have revealed the orientation of the LIPSS can be modified by varying states of laser polarization (linear, circular or elliptical). When a linearly polarized laser beam is applied, the ripples are aligned either perpendicular or parallel to the incident laser polarization [25]. Wang et al. reported that under the irradiation of left and right circularly polarized femtosecond laser pulses the ripples were angled at +45° and −45° with respect to the incident plane of the beam, respectively [25]. On the contrary, the elliptically polarized femtosecond laser pulses induced ripples that were aligned perpendicularly to the long axis, as demonstrated by Tang et al. [26] and Varlamova et al. [27]. Low-spatial frequency LIPSS (LSFL) are observed under specific conditions wherein a spatial periodicity similar to the laser irradiation wavelength is used with an alignment on metals which is perpendicular to the incident laser [23,24]. Originally, it was believed that the ripples generated as a consequence of interference between the incident laser beam and the scattered electromagnetic wave at the surface [23]. Recently, a revised scattering model was proposed by Huang et al. [28] explaining the LIPSS formation in terms of the initial direct surface plasmon (SP)-laser interference and the subsequent grating-assisted SP-laser coupling. The periodicity of these ripples can be altered and controlled by varying laser parameters. Previous studies involving LIPSS have generated ripples on the micrometer scale and have reported equivalent or better cellular responses [16,29,30]. Beyond the viability of cells, studies have reported conflicting results where sub-micron patterns were reported capable of orientating osteoblasts [31] while other studies have only observed visible cell orientation along microscale patterns [16].

In this work, LSFL were generated on the surface of titanium to create sub-micron scale surface topographies. These surfaces were subsequently characterized and evaluated as a potential biomaterial for implant purposes.

2. Methods

2.1. Disk preparation

Titanium disks were prepared by cutting Grade 2 unalloyed sheets of titanium (ASTM-B-265-13A, McMaster-Carr). The sheet was sheared into squares of approximate dimensions of 16 × 16 mm. These squares were subsequently cut using a lathe and blade setup to produce disks with a diameter of 15 mm and a thickness of 1.25 mm.

2.2. Laser ablation

A Yb:KGW femtosecond laser (PHAROS from Light Conversion, Inc) was used to generate linearly polarized laser pulses at a center wavelength of 1030 nm with pulse duration of 300 fs and a repetition rate of 1 kHz to generate LIPSS on the surface of the grade 2 titanium disks in ambient atmosphere. Before laser processing, the samples were ultrasonically cleaned with acetone and ethanol sequentially for 15 min each. The laser beam was perpendicular to the sample surface and focused using a 5× microscope objective lens. The combination of a Glan polarizer and a half wave plate was employed to vary the laser power. The sample was mounted on a computer-controlled xy-translation stage and illuminated from the top to enable monitoring the laser micromachining processes with a CCD camera. The laser ablation process was performed by translating the sample relatively to the stationary laser beam. The focused laser beam radius ω_0 on the Ti sample surfaces (defined at e^{-2} of peak intensity of the Gaussian beam distribution) was determined using the D^2-method developed by Liu [32] to be 10.9 μm. Raster scanning method was applied to achieve complete surface coverage of an area of 10 × 10 mm^2 of titanium samples by scanning a line at a velocity of 1000 μm/s at the laser fluence of 0.5 J/cm^2 and then various lateral displacement of the laser beam of 3 μm, 7.5 μm and 10 μm were applied by translating the stage in a direction perpendicular to the laser beam scanning direction to partially overlap the consecutive laser induced lines to create ripples with periodicities of 300 nm, 620 nm and 760 nm, respectively.

2.3. Characterization

All machined disks were ultrasonically cleaned for 15 min intervals, first in ethanol and then in acetone. Scanning electron microscopy (SEM) images of the laser ablated surfaces were obtained on a JEOL-7000F (JEOL, Peabody, MA) at an accelerating voltage of 2.5 keV. SEM samples were sputter coated with 5 nm of platinum. Atomic force microscopy (AFM) images were acquired on a Bioscope Catalyst (Bruker, Santa Barbara, CA) using the instrument's Scanasyst tapping mode, to both observe the surface modification and to determine surface roughness for each laser-induced periodicity. Water contact angle measurements were determined for all surfaces using a high-speed contact angle measurer, OCA 35 (Future Digital Scientific, Garden City, NY), using a sessile drop method with a droplet size of 3 μL. A JAMP-9500F (JEOL, Peabody, MA) instrument was used to perform Auger electron spectroscopy (AES), at a sputtering rate of approximately 2 nm/s, which allowed for elemental depth profiling of all surfaces.

Sample preparation for transmission electron microscopy (TEM) was done using focused ion beam (FIB) microscope (NVision40, Carl Zeiss AG). An *in situ* lift-out method was used to prepare a TEM lamella less than 100 nm thick. TEM images were acquired on a JEOL 2010F microscope (JEOL, Peabody, MA) using both bright-field and high-angle annular dark-field imaging (HAADF) modes at 200 kV. The microscope is equipped with a Gatan imaging filter (Gatan Inc., Pleasanton, CA) to perform chemical analysis via electron energy loss spectroscopy (EELS). Spectra were initially processed using principal component analysis (PCA) using Digital Micrograph before relevant elemental maps and atomic concentration information were extracted. A power-law background model was used for all shown EELS data.

The periodicity of the laser-ablated disks was determined from SEM images using peak-to-peak measurements in ImageJ (National Institute of Health). Microscope associated software, Nanoscope Analysis (Bruker, Santa Barbara, CA), was used to process and analyze all AFM images. Due to the large variability in roughness of the base titanium substrate, R_{max} was used in lieu of R_a, to better characterize the amount of roughness that was added to the surface as a result of laser ablation.

2.4. Cell culture

Saos-2, osteosarcoma, cells (ATCC ®) were grown in Mccoy's modified 5A media (Life Technologies Inc.) supplemented with 15% fetal bovine serum (Life Technologies Inc.), FBS, and 1% penicillin/streptomycin (Sigma–Aldrich). Cells were kept in an incubator at 37 °C with 5% CO_2 and media was exchanged every 4 days. Upon reaching confluence, cells were detached with trypsin in 0.25% EDTA (Sigma–Aldrich) as per ATCC guidelines and subsequently deactivated with media after confirming detachment via light microscope. Cells were seeded on to the surface of titanium disks (15 mm diameter) placed in a 24 well plate at 10,000 cells/

cm^2. All disks were cleaned in ethanol and acetone as previously outlined before being placed into the cell culture environment. Cells were counted using Countess Automated Cell Counter (Invitrogen™). Cells were allowed to grow on the surface of the disks for up to 14 days with the media changed twice (after 5 and 10 days). 12 samples were used for each surface and time point combination.

2.5. Cell metabolism

Cell metabolism, which can be approximated to cell viability, was measured using the alamarBlue® (Life Technologies Inc.) assay. Media was removed from the wells and replaced with a 350 μL 5% alamarBlue solution (in Mccoy's 5A media) per well. The solution was left to incubate for 1 h in the dark at 37 °C with 5% CO_2. Fluorescence values were read using an Infinite® M1000 (Tecan, Männedorf, Switzerland) at 540–580 nm (excitation-emission). Each well was sampled at 16 points, approximating the well as a 4 × 4 square. The blank reading was subtracted from each data point to obtain the fluorescent signal corresponding to the cell number only. The alamarBlue solution was then removed and 300 μL of 0.1% triton lysis solution (in PBS) was added to each well. Well plates were frozen at −20 °C and freeze-thaw cycles were performed to conduct further assays.

2.6. Alkaline phosphatase activity

Alkaline phosphatase (ALP) activity was measured using the ALP assay (Abcam ®). 50 μL of cell lysis from each well was combined with 100 μL of p-nitrophenol phosphate in assay buffer (Prepared as per Abcam instructions) and allowed to incubate for 20 min in the dark at 37 °C with 5% CO_2. Absorbance was read using Infinite® M1000 (Tecan) at 405 nm. The phosphate group is cleaved by alkaline phosphatase and the resulting p-nitrophenol emits light. Each well was sampled at 16 points, approximating the well as a 4 × 4 square. A standard curve was prepared by using described concentrations of p-nitrophenol (as per Abcam instructions). The blank reading was subtracted from each data point and via the standard curve, absorbance values were converted to p-nitrophenol concentrations.

2.7. Cell orientation

Cells were seeded on the titanium surfaces for 1 day before being fixed with 0.25% glutaraldehyde in a sodium cacodylate buffer. The samples were subsequently stained with osmium tetraoxide before being dehydrated through a series of ethanol rinses starting from 25% (in Milli-Q water) to 100% ethanol. The samples were then critically point dried (Leica Microsystems, Wetzlar, Germany) before being examined under SEM. Stained cell SEM images were acquired on a TESCAN VP. SEM (Tescan, Czech Republic) at an accelerating voltage of 10 keV. Additionally, nuclear area factor and circularity measurements were obtained by relating roundness and area values determined via ImageJ [33]. Circularity and nuclear area factor are unitless measurements determined via ratios of the area and perimeter of cells. Larger values for both are generally associated with healthy cells [33]. A minimum of 3 images was used for all quantitative measurements.

2.8. Statistical analysis

Statistical analysis was performed using the programming language, R (R Core Team, New Zealand), using two-way ANOVA at a significance level of $\alpha = 0.05$ and Tukey's HSD test was used to evaluate contrasts. Data for the cell metabolism and alkaline phosphatase activity was accepted to be normally distributed as per the Shapiro-Wilk test ($p > 0.05$).

3. Results

3.1. Periodicity

Use of the pulsed femtosecond laser successfully generated rippled patterns on the surface of titanium disks which are shown by SEM in Fig. 1. The mean periodicities of 340, 637 and 751 nm for the 300, 620 and 760 nm surfaces were found respectively. These values, along with 95% confidence bounds, are shown in Table 1. In addition to showing that the pattern on the surfaces is consistent, SEM imaging also revealed the presence of nodules, in particular on the 620 nm surface. Resolidified molten material can also be observed on both the 620 and 760 nm surfaces, in the valleys of the rippled pattern. There is also noticeable overlap of the peaks of the rippled pattern on the 300 nm surface.

3.2. Surface roughness

As the titanium disks have an inherent roughness prior to laser ablation, the measurement of interest when considering roughness was the maximum roughness of the rippled pattern generated by the laser. Specifically, this was considered as the difference in height between the peaks and valleys of the rippled pattern (R_{max}). Fig. 1 shows 10 × 10 μm^2 AFM scans of the 300, 620 and 760 nm surfaces. These AFM images confirm the distinct ripple pattern seen in SEM. Measured R_{max} values for each of the laser-ablated surfaces (Table 1) were all found to be in the same general range of 144–163 nm. Due to the inherent roughness of the titanium disks, these images also show variation in surface roughness on the order of approximately 0.5 μm, irrespective of the rippled pattern.

3.3. Additional characterization

Water contact angle measurements for all surfaces are shown in Table 1. These measurements show that the contact angle is larger for all the laser-ablated surfaces with mean values of 109°, 134°, and 132° for the 300, 620, 760 nm surfaces respectively compared to 84° for control surfaces (Fig. 2). AES showed that the estimated oxide thickness of 300, 620 and 760 nm surfaces were 86, 83 and 75% thicker respectively than the control surface (Fig. 3). These percentages can be approximated into relative oxide thickness values which are less than 50 nm (Table 1). The crossover time of oxygen and titanium profiles was used to approximate the thickness of the oxide layer.

3.4. Microstructure analysis

TEM images of the 620 nm surface are given in Fig. 4. Many of the dark lines observed in the images were identified as bend contours via tilting of the sample or as grain boundaries and have been indicated as such in Fig. 4. TEM imaging also revealed that the rippled pattern is not completely uniform due to the presence of partially ablated features on the surface (Fig. 4B). These images also provided a closer look at some of the resolidified molten droplets which have formed into nodules on the surface. Fig. 4C/D show an example SAED pattern taken near the surface of the 620 nm sample which shows that the material has retained a polycrystalline surface layer. Indexing of this pattern, and patterns from other regions of the sample, to determine the specific composition of the oxide was inconclusive.

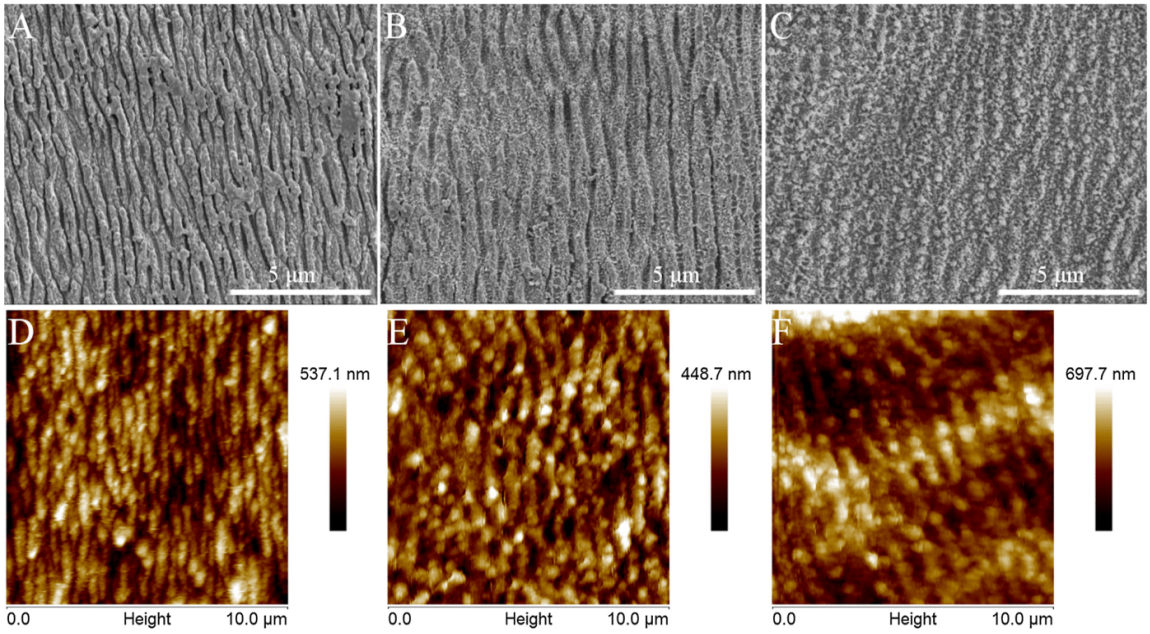

Fig. 1. Scanning electron (A, B, C) and atomic force (D, E, F) micrographs for laser ablated titanium with periodicities of 300, 620 and 760 nm. Periodic patterns have been successfully generated, with consistent laser induced roughness, at all 3 periodicities. (See Table 1 for measured values).

Table 1
Measured periodicity of the ripples, difference in height between the peaks and valleys of the rippled pattern (roughness, R_{max}), water contact angle and relative oxide thickness estimates from AES for all surfaces (300 nm, 620 nm, 760 nm and control) with 95% confidence intervals. The measured periodicities of the surfaces are shown to be very consistent and the laser generated roughness is similar, regardless of the chosen periodicity. The surfaces with larger periodicities demonstrate distinctly hydrophobic behaviour while the control surface is hydrophilic. The oxide thickness estimations show that the laser modified surfaces have a thicker oxide layer compared to the control surface.

Surface	Periodicity (nm)	Roughness (nm)	Contact angle (°)	Oxide thickness (nm)
Control	N/A	N/A	84 ± 3	5
300 nm	340 ± 21	163 ± 4	109 ± 6	37
620 nm	637 ± 8	144 ± 8	134 ± 14	20
760 nm	751 ± 25	155 ± 15	132 ± 5	29

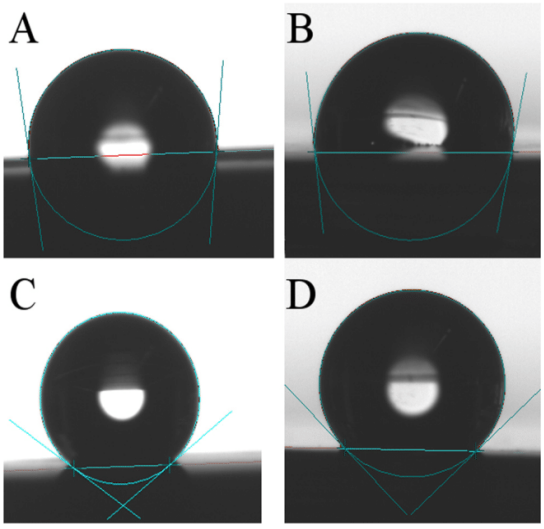

Fig. 2. Demonstration of the different behaviour of milli-q water droplets on the control, 300, 620 and 760 nm (A, B, C & D respectively) substrates. Measured water contact angles were 84, 109, 134 and 132° for the control, 300, 620 and 760 nm substrates respectively. The 620 and 760 nm surfaces demonstrate noticeably more hydrophobic behaviour compared to the control and 300 nm surfaces.

EELS data was able to show the presence of a thin (~35 nm) surface oxide layer. Fig. 5 shows a HAADF image with a corresponding EELS line scan. The line scan shows that the oxygen signal, while present, is extremely minimal in comparison to the titanium signal and the estimated oxide thickness is comparable to what was observed in AES. The EELS spectrum map shown in Fig. 5 provides additional support to the thin oxide layer as the concentrated or bright green regions of oxygen are only present along the surface of the sample.

3.5. Cell metabolism

The cell metabolism results in Fig. 6A directly correlate fluorescence to cell metabolism. For each surface, from 3 to 7 days, the magnitude of cell metabolism increased for each surface but was only statistically significant for the 760 nm surface ($p < 0.05$). There were no statistically significant differences noted between 7 and 14 days for any of the individual surfaces. At the 3 day time point, both the 620 nm and control surfaces show statistically significant increases in metabolism compared to the 300 nm surface. This effect extends to the 7 day time point for the control surface. The control surface also showed statistically significant increases in metabolism compared to the 760 nm surface after 3 days. However, all of these effects disappear after 14 days.

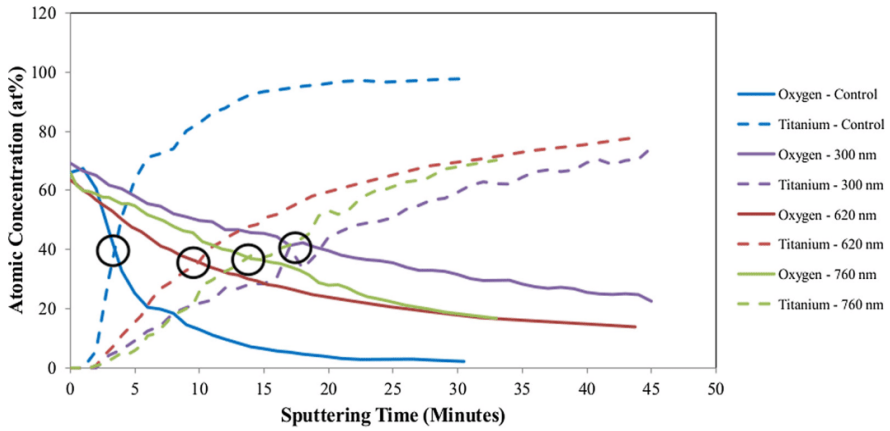

Fig. 3. Auger electron spectroscopy (AES) depth profiles for control and laser ablated (300 nm, 620 nm and 760 nm) surfaces. Profiles reveal that the oxide layer for all laser ablated surfaces are thicker than the unmodified titanium. Relative oxide layer thickness estimates were obtained by comparing the crossover times (circled intersections of Ti and O profiles) between the laser ablated surfaces and controls (See Table 1 for values), where a crossover at longer sputtering times represents a larger oxide thickness.

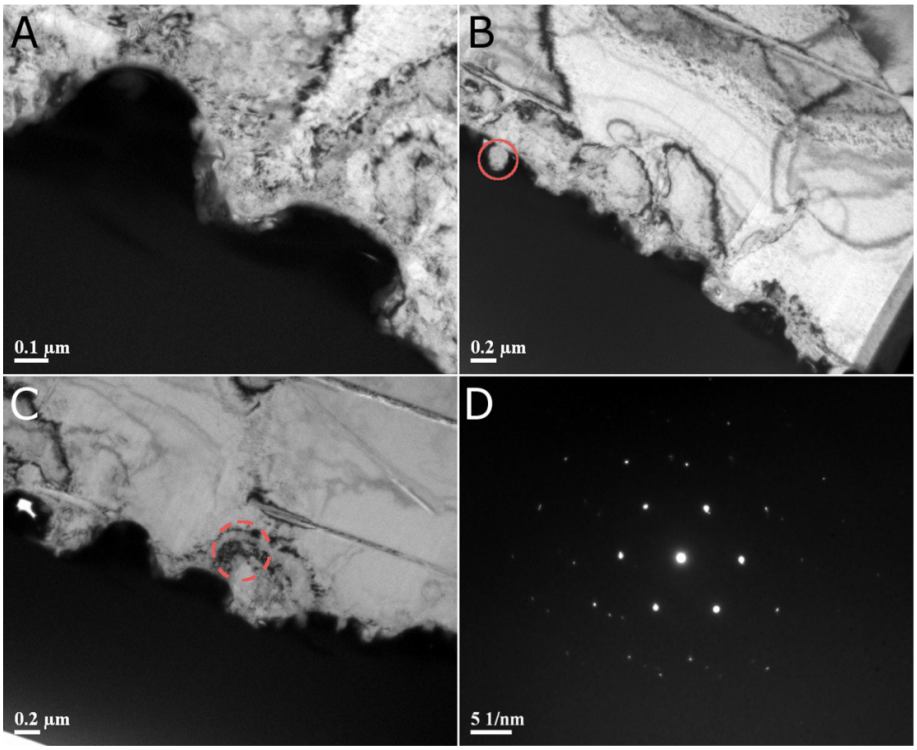

Fig. 4. Cross-sectional TEM micrographs of the 620 nm surface (A, B) showing the generated rippled pattern while revealing the presence of additional surface features (circle – resolidified molten droplet, arrowhead – contour line, solid arrow – grain boundary). Diffraction pattern (D) taken from the surface of the substrate (C) reveals a polycrystalline surface layer.

3.6. Alkaline phosphatase activity

Alkaline phosphatase activity for each surface after 3, 7 and 14 days of cell seeding time is shown in Fig. 6B. Similar to cell metabolism, the magnitude of alkaline phosphatase activity increased from 3 to 7 days but was only statistically significant for the 620 nm and control surfaces ($p < 0.05$). Notably, the alkaline phosphatase activity on the control surface showed a statistically significant decrease from 7 to 14 days. However, no corresponding decrease in cell metabolism was observed. Similarly, a statistically significant difference between both the 620 and 760 nm surfaces and the control surface after 14 days of cell seeding was noted. Additionally, the 620 nm surface showed statistically significant increases at the 3 day time point compared to the 760 nm surface.

3.7. Cell orientation

SEM images of Saos-2 cells on laser-ablated and control surfaces can be observed in Fig. 7. This shows that the cells on the laser ablated surface have an elongated phenotype compared to the cells

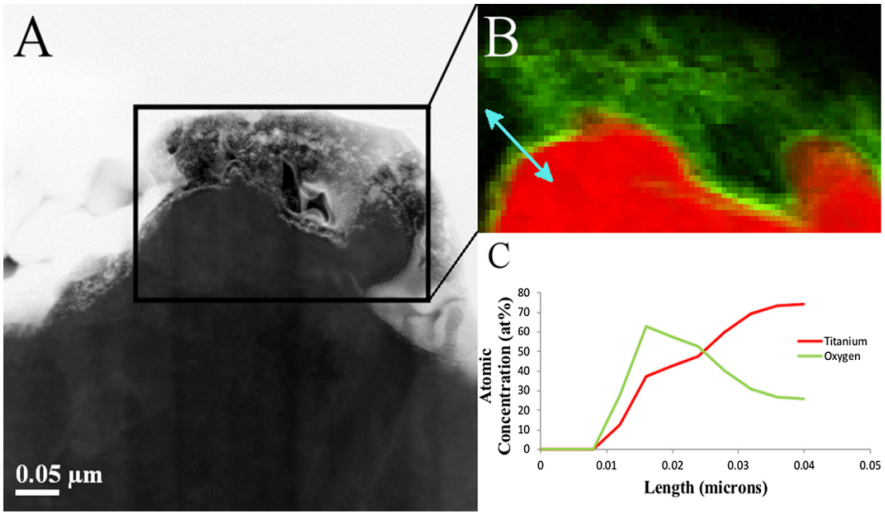

Fig. 5. EELS line scan (C) with accompanying HAADF image (A) of the 620 nm surface. EELS spectrum colour map (B) for a nodule on the 620 nm surface. The red indicates the titanium while the green indicates the oxygen. The presence of high concentrations of oxygen can only be seen at the surface of the substrate. The line scan (C; double-sided blue arrow) reveals a higher concentration of oxygen over a small length and supports AES estimates that the oxide layer is 20–30 nm in thickness.

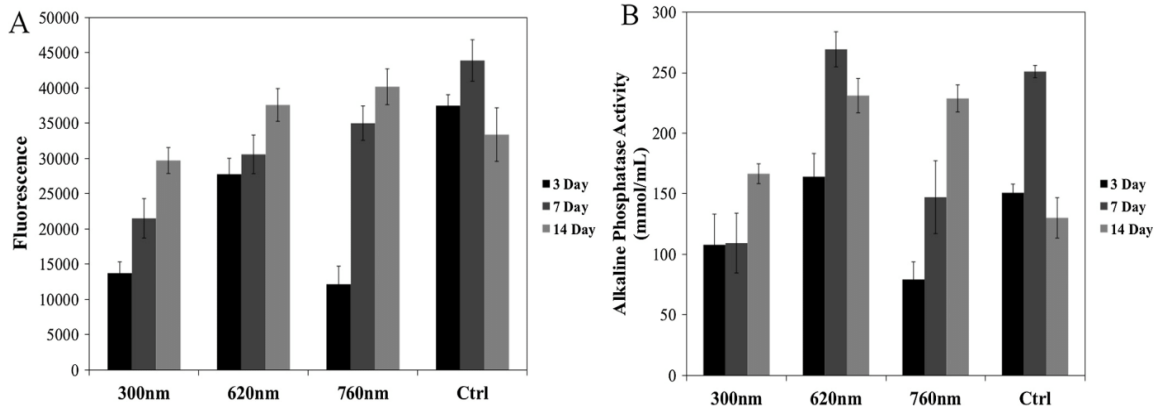

Fig. 6. (A) Cell metabolism at early time points was significantly greater on the control surface than the 300 and 760 nm surfaces but this effect disappeared at later time points. The 620 nm surface had statistically significant increased metabolism after 3 days compared to 300 and 760 nm surfaces and after 7 days compared to the 300 nm surface. At late time points there was no difference between the laser modified surfaces and controls. Error bars represent standard error. (B) ALP activity [mmol/mL] for control and laser modified surfaces. The 620 nm surface had statistically significant ($p < 0.05$) improvements in ALP activity at 3 and 7 days compared to the 760 nm surface. The 620 and 760 nm surfaces had statistically significant ($p < 0.05$) improvements in ALP activity after 14 days compared to the control surface. Error bars represent standard error.

on the unmodified titanium surface. The cells on the laser ablated surfaces appear to be oriented perpendicular to the periodic structures which can be observed in Fig. 7C/D. Fig. 7D shows that many of the filopodia have attached directly to the peaks of the rippled pattern. The circularity and nuclear area factor, a common indicator of cell health, are listed in Table 2. The circularity of the cells is higher on the control surface compared to the laser-ablated surfaces while the average nuclear area factor is larger for cells on the laser-ablated surfaces. These effects were only noticeable at lower seeding densities, confluent layers displayed no detectable differences in orientation or circularity (results not shown).

4. Discussion

The generation of ripples using a femtosecond laser allowed for a specific and ordered surface modification of titanium for implant purposes. These patterns are consistent and significantly differentiate themselves from more random or disorganized modification techniques. This is potentially advantageous in industrial or clinical settings as the consistency observed in the periodicity measurements is promising from a quality-control standpoint. The ripples generated visibly distinguish themselves from unmodified titanium and, with regards to periodicity, are similar in appearance to that of collagen fibrils. TEM imaging revealed the presence of grain boundaries and bend contours, the grains were noted to be smaller towards the surfaces compared to the bulk material. This effect has been noted previously where grain size distributions were observed at the surface of femtosecond treated materials [34]. In addition, this refined grain structure may contribute to a tougher surface coating [35]. The observed nodules are likely resolidified molten droplets from the laser ablation process which may benefit biological adhesion by increasing surface contact area.

Results showed that the laser ablation had effects on both the surface chemistry and topography that warrant discussion. Firstly,

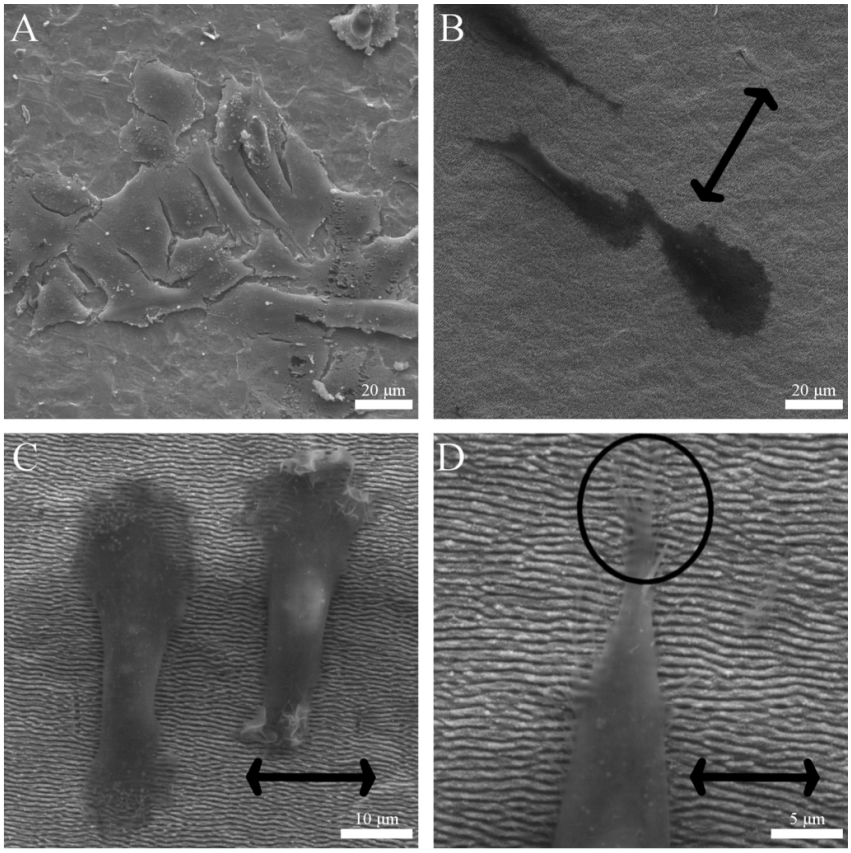

Fig. 7. SEM images of fixed and stained Saos-2 cells on control (A) and laser modified surfaces (B; 300 nm ripples, C and D; 620 nm ripples) after 1 day of seeding. The cells on the laser ablated surfaces appear to be perpendicularly aligned with the periodic structures (B, C, D). (D) shows interactions with the filopodia of the cells with the peaks of the rippled pattern. Double-sided arrows indicate the direction of the periodic patterns while the circle in (D) indicates filopodia attachments.

Table 2
Average circularity and nuclear area factor of cells fixed on to 300, 620, 760 nm and control surfaces. Measurements were obtained from SEM images via ImageJ, a minimum of 3 images was used for each parameter. Circularity was lower for the laser-ablated surfaces compared to the control while the nuclear area factor was higher for the laser-ablated surfaces compared to the control.

Surface	Circularity	Nuclear Area Factor
Control	0.45	152
300 nm	0.33	432
620 nm	0.32	302
760 nm	0.11	239

all modified surfaces showed a very consistent roughness resulting from the laser modification. These roughness values, like with the periodicity measurements, were very consistent regardless of chosen periodicity and this shows that the modification technique is easily reproduced. This is a positive result as one of the main limitations to understanding sub-micron topographies is the lack of consistency in the preparation of the surfaces [36,37]. In terms of magnitude, the roughness values for the laser modified surfaces and the base titanium substrate were on the submicron and micron scale respectively. This resulting dual-stage roughness ultimately increases the surface area which is good from an osseointegration standpoint [21,37]. Additionally, the laser-ablated surface was found to be significantly more hydrophobic than unmodified controls. It should be noted that the 300 nm surface was less hydrophobic compared to the 620 and 760 nm surfaces. Preference, when considering biomaterials, is given to hydrophilic surfaces to allow for greater interaction between material and the *in vivo* environment as a hydrophobic surface has the potential of leading to isolation of the material via thrombosis or similar pathways [38,39]. Chemical analysis revealed that the naturally occurring oxide layer of titanium on modified surfaces was still present and noticeably thicker in magnitude compared to the control surface. This was confirmed via results from AES and EELS. It was expected that the laser ablation would increase the overall thickness of the oxide layer due to the laser ablation occurring in air. This is beneficial because this naturally occurring oxide layer is known to be a major contributing factor to titanium's position as a favourable biomaterial for osseointegration. It has been previously reported that thicker, more uniform oxide layers are more stable compared to natural titanium which has a relatively thin, defect-heavy oxide layer [40,41].

Evaluation of the surface from *in vitro* testing showed that the laser modified surface allowed for cell metabolism and subsequently alkaline phosphatase activity. As expected, both of the measured parameters showed an increase in magnitude with increasing cell-seeding time. When considering seeding time, only

the 760 nm surface showed statistically significant increases in cell metabolism from 3 to 7 days. However, by 14 days all statistically significant effects disappear and there is no difference between the four surfaces. From an osseointegration standpoint this is positive as it demonstrates that all the modified surfaces are not cytotoxic and do not down-regulate cell growth or proliferation. These results have shown that the cells are capable of exhibiting typical cell growth behaviour from log to stationary phases. It was previously observed by Raimbault et al. that micron-sized ripples showed no difference compared to control surfaces with regard to cell growth [16]. This work used sub-micron ripples and a similar outcome has been observed. Statistically significant increases in alkaline phosphatase activity were observed for each surface except for the 300 nm from 3 to 7 days which corresponded to the increased metabolism observed over time. Interestingly, there was a statistically significant decrease in alkaline phosphatase activity in the control group from 7 to 14 days and there was no corresponding decrease in metabolism. This was not an effect that was observed for the laser-ablated surfaces. In fact, the 620 and 760 nm surfaces showed improved alkaline phosphatase activity compared to the control group at 14 days. This decrease in ALP activity may have resulted from cells on the control surface at 14 days entering the death phase of cell growth which may have reduced the overall ALP activity measurement. The decreased circularity of cells observed on the laser ablated surface compared to the control surface show that the cells have a greater spread, which has been associated with improved cell health [42–44]. Lower nuclear area factor has been shown to be a strong indicator of cell apoptosis [33], [45]. While the *in vitro* assays show that cell apoptosis is not prevalent during the examined timeframe, the increased nuclear area factor of cells observed on the laser-ablated surfaces suggests that these cells may be relatively healthier. SEM images of fixed cells on the laser ablated surfaces show that the filopodia of the cells appear to be attaching to the peaks of the laser ablated pattern. It has been shown by Dalby et al. that there is a response between filopodia and features as small as 10 nm [42,46,47]. This suggests that the laser ablated features may experience nanocontact guidance which is why the cells on the laser-ablated surfaces showed reduced circularity compared to the control surface.

Overall, the 620 nm surface performed better than the other laser-ablated surfaces in terms of cell metabolism and alkaline phosphatase at all time points. The 620 nm surface also showed statistically significant increased alkaline phosphatase activity compared to the control surface. This suggests that the surface modification may have an effect on adherent Saos-2 cells. Studies have shown that different cells tend to prefer different sized features when considering their growth and proliferation on biomaterials [16,48,49]. Saos-2 cells are of similar length scale to osteoblasts, so their behaviour on the laser-ablated surfaces can be considered an appropriate model of osteoblast adhesion [50]. It is noteworthy that the 300 nm surface, the laser-ablated surfaces with the thickest estimated oxide layer and the least hydrophobic, performed the worst when considering the *in vitro* studies. This leads to suspicion from the authors that the difference in wettability between the laser-ablated surfaces is not significant or that the generated rippled pattern, and its corresponding change to the surface roughness, is counterbalancing these alterations. It should also be noted that this study primarily focused on early osseointegration. From that perspective, the 620 nm and control surfaces performed the best. Thus, when evaluating the 300 and 760 nm surfaces, it should be noted that tests associated with long-term osseointegration or *in vivo* studies have shown that nanoscale roughness is beneficial [51–53].

Additional studies on these laser-modified surfaces are needed to completely understand how the contrasting effects of surface topography and chemistry are affecting cell adhesion, metabolism and proliferation. Additional *in vitro* studies with different cell lines, perhaps non-osteoblast-like, may be necessary to understand the specific adhesion and proliferation mechanics in place. Finally, i*n vivo* studies are a logical next step to further investigate the osseointegration ability of the laser modified surfaces over longer times in a more clinically relevant scenario.

5. Conclusions

The use of a pulsed femtosecond laser to generate reproducible and sub-micron patterns using laser-ablation methods on titanium substrates was successfully demonstrated. The surfaces were consistent with regards to periodicity, laser-induced roughness and oxide thickness. Of the three designed periodicities, the 620 nm surface showed improved capacity as an implant surface from a biocompatibility standpoint. This study has demonstrated the potential of using LIPSS to generate potentially biologically relevant patterns that may have potential for titanium modification in orthopaedic or dental implant applications.

Acknowledgements

We would like to acknowledge the support of the Natural Sciences and Engineering Research Council of Canada (NSERC) and the Discovery Grant Program (RGPIN 2014-06053). Microscopy was carried out at the Canadian Centre for Electron Microscopy, a facility supported by NSERC and other government agencies. *In vitro* studies were performed at the Biointerfaces Institute at McMaster University.

Conflict of interest

The authors declare no conflict of interest.

References

[1] T. Albrektsson, Osseointegrated Titanium Implants, 1981, pp. 155–170.
[2] B.D. Boyan, T.W. Hummert, D.D. Dean, Z. Schwartz, Role of material surfaces in regulating bone and cartilage cell response, Biomaterials 17 (2) (1996) 137–146.
[3] S.F. Hulbert, F.W. Cooke, J.J. Klawitter, R.B. Leonard, B.W. Sauer, D.D. Moyle, Attachment of prostheses to the musculo-skeletal system by tissue ingrowth and mechanical interlocking, J. Biomed. Mater. Res. 23 (4) (1973) 1–23.
[4] F. Guillemot, F. Prima, V.N. Tokarev, C. Belin, M.C. Port-Durrieu, T. Gloriant, C. Baquey, S. Lazare, Single-pulse KrF laser ablation and nanopatterning in vacuum of beta-titanium alloys used in biomedical applications, Appl. Phys. A 79 (4–6) (2004) 811–813.
[5] D.S. Milovanović, S.M. Petrović, M.a. Shulepov, V.F. Tarasenko, B.B. Radak, Š.S. Miljanic, M.S. Trtica, Titanium alloy surface modification by excimer laser irradiation, Opt. Laser Technol. 54 (2013) 419–427.
[6] D.S. Milovanović, B.B. Radak, B.M. Gaković, D. Batani, M.D. Momčilović, M.S. Trtica, Surface morphology modifications of titanium based implant induced by 40picosecond laser pulses at 266nm, J. Alloys Compd. 501 (1) (2010) 89–92.
[7] Y.S. Tian, C.Z. Chen, S.T. Li, Q.H. Huo, Research progress on laser surface modification of titanium alloys, Appl. Surf. Sci. 242 (1–2) (2005) 177–184.
[8] M. Trtica, B. Gakovic, D. Batani, T. Desai, P. Panjan, B. Radak, Surface modifications of a titanium implant by a picosecond Nd:YAG laser operating at 1064 and 532nm, Appl. Surf. Sci. 253 (5) (2006) 2551–2556.
[9] N.B. Kurella, A. Dahotre, Review paper: surface modification for bioimplants: the role of laser surface engineering, J. Biomater. Appl. 20 (1) (2005) 5–50.
[10] G. Passeri, A. Cacchioli, F. Ravanetti, C. Galli, E. Elezi, G.M. Macaluso, Adhesion pattern and growth of primary human osteoblastic cells on five commercially available titanium surfaces, Clin. Oral Implants Res. 21 (7) (2010) 756–765.
[11] H. Solař, P. Kylián, O. Marek, A. Vandrovcová, M. Bacáková, L. Hanuš, J. Biederman, Particles induced surface nanoroughness of titanium surface and its influence on adhesion of osteoblast-like MG-63 cells, Appl. Surf. Sci. 324 (2015) 99–105.
[12] E.M. Lotz, R. Olivares-Navarrete, S. Berner, B.D. Boyan, Z. Schwartz, Osteogenic response of human MSCs and osteoblasts to hydrophilic and hydrophobic nanostructured titanium implant surfaces, J. Biomed. Mater. Res. Part A (2016) 1–12.
[13] C. Larsson, P. Thomsen, B.O. Aronsson, M. Rodahl, J. Lausmaa, B. Kasemo, L.E. Ericson, Bone response to surface-modified titanium implants: studies on the

early tissue response to machined and electropolished implants with different oxide thicknesses, Biomaterials 17 (6) (Mar. 1996) 605–616.
[14] B.E.J. Lee, S. Ho, G. Mestres, M. Karlsson Ott, P. Koshy, K. Grandfield, Dual-topography electrical discharge machining of titanium to improve biocompatibility, Surf. Coatings Technol. 296 (2016) 149–156.
[15] A.Y. Vorobyev, C. Guo, Femtosecond laser structuring of titanium implants, Appl. Surf. Sci. 253 (17) (2007) 7272–7280.
[16] O. Raimbault, S. Benayoun, K. Anselme, C. Mauclair, T. Bourgade, A.-M. Kietzig, P.-L. Girard-Lauriault, S. Valette, C. Donnet, The effects of femtosecond laser-textured Ti-6Al-4V on wettability and cell response, Mater. Sci. Eng. C 69 (2016) 311–320.
[17] M. Kreisler, H. Al Haj, H. Götz, H. Duschner, B. D'Hoedt, Effect of simulated CO_2 and GaAlAs laser surface decontamination on temperature changes in Ti-plasma sprayed dental implants, Lasers Surg. Med. 30 (3) (2002) 233–239.
[18] E. Mariscal-Muñoz, C.A.S. Costa, H.S. Tavares, J. Bianchi, J. Hebling, J.P.B. Machado, U.H. Lerner, P.P.C. Souza, Osteoblast differentiation is enhanced by a nano-to-micro hybrid titanium surface created by Yb:YAG laser irradiation, Clin. Oral Investig. 20 (3) (2016) 503–511.
[19] M. Radmanesh, A.M. Ektesabi, R.A. Wyatt, B.D. Crawford, A. Kiani, Mouse embryonic fibroblasts accumulate differentially on titanium surfaces treated with nanosecond laser pulses, Biointerphases 11 (3) (2016) 31009.
[20] R. Brånemark, L. Emanuelsson, A. Palmquist, P. Thomsen, Bone response to laser-induced micro- and nano-size titanium surface features, Nanomed. Nanotechnol., Biol. Med. 7 (2) (2011) 220–227.
[21] F.A. Shah, M.L. Johansson, O. Omar, H. Simonsson, A. Palmquist, P. Thomsen, Laser-modified surface enhances osseointegration and biomechanical anchorage of commercially pure titanium implants for bone-anchored hearing systems, PLoS One 11 (6) (2016) 1–24.
[22] C. Hallgren, H. Reimers, D. Chakarov, J. Gold, A. Wennerberg, An in vivo study of bone response to implants topographically modified by laser micromachining, Biomaterials 24 (5) (2003) 701–710.
[23] J.E. Sipe, J.F. Young, J.S. Preston, H.M. Van Driel, Laser-induced periodic surface structure. I. Theory, Phys. Rev. B 27 (2) (1983) 1141–1154.
[24] J.F. Young, J. Preston, H. Van Driel, J. Sipe, Laser induced periodic surface structures II. Experiments on Ge, Si, Al and brass, Phys. Rev. B 27 (2) (1983) 1155.
[25] J. Wang, C. Guo, Permanent recording of light helicity on optically inactive metal surfaces, Opt. Lett. 24 (2006) 3641–3643.
[26] Y. Tang, J. Yang, B. Zhao, M. Wang, X. Zhu, Control of periodic ripples on metals by femtosecond laser ellipticity, Opt. Express 23 (2012) 25826–25833.
[27] O. Varlamova, F. Costache, M. Ratzke, J. Reif, Control parameters in pattern formation upon femtosecond laser ablation, Appl. Surf. Sci. 253 (2007) 7932–7936.
[28] M. Huang, F. Zhao, Y. Cheng, N. Xu, Z. Xu, Origin of laser-induced near-subwavelength ripples: interference between surface plasmons and incident laser, ACS Nano 3 (2009) 4062–4070.
[29] M.C. Cunha, A. Zouani, O.F. Plawinski, L. Do Rego, A.M.B. Almeida, A. Vilar, R. Durrieu, Human mesenchymal stem cell behavior on femtosecond laser-textured Ti-6Al-4V surfaces, Nanomedicine 10 (5) (2015) 725–739.
[30] P. Bizi-Bandoki, S. Benayoun, S. Valette, B. Beaugiraud, E. Audouard, Modifications of roughness and wettability properties of metals induced by femtosecond laser treatment, Appl. Surf. Sci. 257 (12) (2011) 5213–5218.
[31] T. Shinonaga, M. Tsukamoto, T. Kawa, P. Chen, A. Nagai, T. Hanawa, Formation of periodic nanostructures using a femtosecond laser to control cell spreading on titanium, Appl. Phys. B Lasers Opt. 119 (3) (2015) 493–496.
[32] J.M. Liu, Simple technique for measurements of pulsed Gaussian-beam spot sizes, Opt. Lett. 7 (1982) 196–198.
[33] M.a. DeCoster, The Nuclear Area Factor (NAF): a measure for cell apoptosis using microscopy and image analysis, Mod. Res. Educ. Top. Microsc. (2007) 378–384.
[34] M.V. Shugaev, C. Wu, O. Armbruster, A. Naghilou, N. Brouwer, D.S. Ivanov, T.J.-Y. Derrien, N.M. Bulgakova, W. Kautek, B. Rethfeld, L.V. Zhigilei, Fundamentals of ultrafast laser–material interaction, MRS Bull. 41 (12) (2016) 960–968.
[35] S. Zhang, D. Sun, Y. Fu, H. Du, Recent advances of superhard nanocomposite coatings: a review, Surf. Coatings Technol. 167 (2–3) (2003) 113–119.
[36] L. Le Guéhennec, A. Soueidan, P. Layrolle, Y. Amouriq, Surface treatments of titanium dental implants for rapid osseointegration, Dent. Mater. 23 (7) (2007) 844–854.
[37] M.M. Shalabi, A. Gortemaker, M.A. Van't Hof, J.A. Jansen, N.H.J. Creugers, Implant surface roughness and bone healing: a systematic review, J. Dent. Res. 85 (6) (2006) 496–500.
[38] M. Chiapasco, F. Biglioli, L. Autelitano, E. Romeo, R. Brusati, Clinical outcome of dental implants placed in fibula-free flaps used for the reconstruction of maxillo-mandibular defects following ablation for tumors or osteoradionecrosis, Clin. Oral Implants Res. 17 (2) (2006) 220–228.
[39] P. Thevenot, W. Hu, L. Tang, Surface chemistry influences implant biocompatibility, Curr. Top. Med. Chem. 8 (4) (2008) 270–280.
[40] N. Huang, P. Yang, Y.X. Leng, J.Y. Chen, H. Sun, J. Wang, G.J. Wang, P.D. Ding, T.F. Xi, Y. Leng, Hemocompatibility of titanium oxide films, Biomaterials 24 (13) (2003) 2177–2187.
[41] J. Pouilleau, D. Devilliers, F. Garrido, S. Durand-Vidal, E. Mahé, Structure and composition of passive titanium oxide films, Mater. Sci. Eng. B 47 (3) (1997) 235–243.
[42] M.J. Dalby, M.O. Riehle, H.J.H. Johnstone, S. Affrossman, A.S.G. Curtis, Polymer-demixed nanotopography: control of fibroblast spreading and proliferation, Tissue Eng. 8 (6) (2002) 1099–1108.
[43] P. Brun, M. Scorzeto, S. Vassanelli, I. Castagliuolo, G. Palù, F. Ghezzo, G.M.L. Messina, G. Iucci, V. Battaglia, S. Sivolella, A. Bagno, G. Polzonetti, G. Marletta, M. Dettin, Mechanisms underlying the attachment and spreading of human osteoblasts: from transient interactions to focal adhesions on vitronectin-grafted bioactive surfaces, Acta Biomater. 9 (4) (2013) 6105–6115.
[44] J. Schwartz, M.J. Avaltroni, M.P. Danahy, B.M. Silverman, E.L. Hanson, J.E. Schwarzbauer, K.S. Midwood, E.S. Gawalt, Cell attachment and spreading on metal implant materials, Mater. Sci. Eng. C 23 (3) (2003) 395–400.
[45] I.M. Helmy, A.M. Abdel Azim, Efficacy of ImageJ in the assessment of apoptosis, Diagn. Pathol. 7 (1) (2012) 15.
[46] M.J. Dalby, M.O. Riehle, H. Johnstone, S. Affrossman, A.S.G. Curtis, Investigating the limits of filopodial sensing: A brief report using SEM to image the interaction between 10 nm high nano-topography and fibroblast filopodia, Cell Biol. Int. 28 (3) (2004) 229–236.
[47] M.J. Dalby, N. Gadegaard, M.O. Riehle, C.D.W. Wilkinson, A.S.G. Curtis, Investigating filopodia sensing using arrays of defined nano-pits down to 35 nm diameter in size, Int. J. Biochem. Cell Biol. 36 (10) (2004) 2015–2025.
[48] P.M. Davidson, M. Bigerelle, G. Reiter, K. Anselme, Different surface sensing of the cell body and nucleus in healthy primary cells and in a cancerous cell line on nanogrooves, Biointerphases 10 (3) (2015) 31004.
[49] M. Eichhorn, C. Stannard, K. Anselme, J. Rühe, Nucleus deformation of SaOs-2 cells on rhombic μ-pillars, J. Mater. Sci. Mater. Med. 26 (2) (2015) 1–6.
[50] C. Pautke, M. Schieker, T. Tischer, A. Kolk, P. Neth, W. Mutschler, S. Milz, Characterization of osteosarcoma cell lines MG-63, Saos-2 and U-2 OS in comparison to human osteoblasts, Anticancer Res. 24 (6) (2004) 3743–3748.
[51] L. Salou, A. Hoornaert, G. Louarn, P. Layrolle, Enhanced osseointegration of titanium implants with nanostructured surfaces: an experimental study in rabbits, Acta Biomater. 11 (1) (2015) 494–502.
[52] S.L. Hyzy, A. Cheng, D.J. Cohen, G. Yatzkaier, A.J. Whitehead, R.M. Clohessy, R.A. Gittens, B.D. Boyan, Z. Schwartz, Novel hydrophilic nanostructured microtexture on direct metal laser sintered Ti-6Al-4V surfaces enhances osteoblast response in vitro and osseointegration in a rabbit model, J. Biomed. Mater. Res. – Part A 104 (8) (2016) 2086–2098.
[53] D. Karazisis, A.M. Ballo, S. Petronis, H. Agheli, L. Emanuelsson, P. Thomsen, O. Omar, The role of well-defined nanotopography of titanium implants on osseointegration: cellular and molecular events in vivo, Int. J. Nanomedicine 11 (2016) 1367–1382.

Chapter 4

This chapter is based on the following published paper:

Mechanism of Superhydrophilic to Superhydrophobic Transition of Femtosecond Laser-Induced Periodic Surface Structure on Titanium (Publication 2)

Hourieh Exir, and Arnaud Weck, "Mechanism of Superhydrophilic to Superhydrophobic Transition of Femtosecond Laser-Induced Periodic Surface Structure on Titanium", Surf. Coat. Tech. 378 (2019) 124931.

4.1 Author contribution:

H. Exir conceived the idea of this work. The results came from experiments designed and performed by H. Exir at the University of Ottawa. The femtosecond laser micromachining of the samples were performed by H. Exir at the Fracture and Femtosecond Research Ottawa Group (FROG) lab of professor Weck, University of Ottawa. All the characterizations and detailed analysis of the data were conducted by H. Exir. The manuscript was written by H. Exir. All authors contributed to the final manuscript.

Abstract

The wettability is an imperative property of a solid surface. For decades, superhydrophobic and superhydrophilic surfaces have been focus of extensive research owing to their importance for both fundamental research and in many biomedical, aeronautical, and industrial applications. There have been many studies reported on wettability transition of micro- and nanostructured metal surfaces over time, but there seems to be no well-accepted mechanism to address this phenomenon. Therefore, a detailed study of the surface chemical composition of the laser ablated surfaces at different time points is necessary to develop an understanding of the factors resulting in change in wettability over time. The aim of the present work was to investigate the mechanism underlying the wettability transition of femtosecond laser generated periodic surface structures on titanium between the superhydrophilic and superhydrophobic wetting states under ambient conditions. The time-dependent wettability of the laser treated surfaces assessed by the sessile drop method. The samples exhibited superhydrophilic behavior immediately after laser texturing and became superhydrophobic over time. Detailed surface chemical analyses by X-ray photoelectron spectroscopy revealed that the unique electronic structures of Ti_2O_3 and TiO_2 and resulting in hydrophilic and hydrophobic hydration structures, respectively, played a crucial role in the observed wettability transition.

Keywords*:* Surface chemistry; Femtosecond laser; Titanium; Wettability transition; Superhydrophilicity; Superhydrophobicity

1. Introduction

The surfaces with superhydrophilic (water contact angle (WCA) $<5^{o}$) and superhydrophobic (WCA$>150^{o}$ and sliding angle (SA) $<10^{o}$) property [1-4] exhibit a variety of important applications including in anti-corrosion [5-7], self-cleaning surfaces [8, 9], anti-icing [10-12], and anti-microbial [13]. The wetting state is controlled through the topography and chemical composition of the surface [14, 15]. Several techniques have been applied to alter the chemistry and morphology of solid surfaces including lithography [16], plasma treatment [17], chemical etching [18], electrodeposition [19] and chemical vapor deposition [20]. During the last decade, femtosecond (fs) lasers have emerged as a simple, high resolution, fast, controllable, reproducible, contactless, single step processing technique applicable to a wide class of materials, including metals [21], semiconductors [22], and polymers [23], by generating spatially periodic structures known as laser-induced periodic surface structures (LIPSS) or ripples. The formation of the periodic ripples with spatial periods close to the wavelength of the laser was attributed to the interference between the incident laser beam and the surface scattering wave [24]. Recently, a revised scattering model was proposed [25] explaining the formation of ripples in terms of the initial direct surface plasmon (SP)-laser interference and the subsequent grating-assisted SP-laser coupling. High biocompatibility, corrosion resistance, and strength to weight ratio have led Titanium (Ti) to be successfully used in many biomedical, aeronautical, and industrial applications [26, 27]. Numerous studies have demonstrated the critical role the surface wettability of the biomaterials plays in regulating the important physiological processes such as protein adsorption, cell adhesion, and cell proliferation [28, 29].

There have been many studies reported on wettability transition of laser induced micro- and nanostructured metal oxide surfaces exhibiting hydrophilicity (WCA$<90^{o}$) or superhydrophilicity immediately after laser ablation and becoming hydrophobic ($90^{o}<$WCA$<150^{o}$) or even superhydrophobic over time in ambient air [30, 31] without using a coating. Several mechanisms have been proposed to explain this observed time dependent wetting transition phenomenon. Kietzig et al. [30] suggested that the catalyzed decomposition of carbon dioxide into carbon on laser-produced active magnetite was responsible for the observed wettability transition of the laser ablated metal alloy surfaces

showing superhydrophilic behavior immediately after laser irradiation and subsequently becoming superhydrophobic over time in air. Long et al. [31] indicated that the picosecond laser textured copper surface showed hydrophilicity immediately after laser ablation and eventually becoming hydrophobic over time in ambient air. The latter conversion in the wettability was stated to be due to the hydrocarbon adsorption over time upon air exposure. There seems to be no well-accepted mechanism to address the wettability transition of the laser ablated surfaces over time. Therefore, for a comprehensive understanding of the factors resulting in wettability changes over time, a detailed study of the surface chemical composition of laser ablated surfaces at different time points is necessary.

In the present study, the mechanism underlying the wetting transition of fs laser generated LIPSS on grade 2 Ti was systematically assessed by analyzing the surface chemical compositions of three surfaces: the fresh laser textured surface, and laser textured surfaces aged under ambient conditions for 45 days and a year. Immediately after laser texturing, the Ti surface showed superhydrophilicity then the WCAs of these surface gradually increased over time until the surface turned superhydrophobic after aging for a year under ambient conditions, without applying any chemical treatment to the surface. The surface chemical analysis results revealed the unique electronic structure of TiO_2 and Ti_2O_3 resulting in hydrophobic and hydrophilic hydration structures, respectively, playing a significant role in the wetting transition. Moreover, the increase of surface nonpolarity due to the accumulation of organic matters absorbed from the air over time has contributed to the observed superhydrophobicity. According to Wenzel [14] and Cassie-Baxter [15] theories, the increase of surface roughness on Ti surfaces by LIPSS had an amplification effect on wettability behavior of laser textured surfaces. The wettability evolution mechanism is thoroughly elaborated in section 3.4.

2. Experimental

2.1. Materials

All the Ti substrates used in this study were made from commercially pure Ti (99%, Grade 2) obtained from McMaster-Carr. The Ti sheet was cut into dimensions of 12×12×0.9 mm^3. The deionized water used as the probe liquid in WCA measurements was purchased

from Sigma Aldrich. The substrates were ultrasonically cleaned for 15 minutes in successive baths of acetone and ethanol before laser treatment.

2.2. Femtosecond laser processing

A Yb:KGW fs (PHAROS from Light Conversion, Inc) was used to generate linearly polarized laser pulses at a center wavelength of 1030 nm with pulse duration of 300 fs and a repetition rate of 1kHz to generate LIPSS on the surface of the grade 2 titanium squares in ambient atmosphere. The laser beam was perpendicular to the sample surface and focused using a 5x microscope objective lens. The combination of a Glan polarizer and a half wave plate was employed to vary the laser power. The sample was mounted on a computer-controlled xy-translation stage and illuminated from the top to enable monitoring the laser micromachining processes with a CCD camera. The laser ablation process was performed by translating the sample relatively to the stationary laser beam. The focused laser beam radius ω_0 on the Ti sample surfaces (defined at e^{-2} of peak intensity of the Gaussian beam distribution) was determined using the D^2-method to be 10.9 μm. Raster scanning method was applied to achieve complete surface coverage of an area of 10x10 mm^2 of titanium samples by scanning a line at a velocity of 1000 μm/s at the laser fluence of 0.5 J/cm^2 and lateral displacement of the laser beam of 7.5 μm was applied by translating the stage in a direction perpendicular to the laser beam scanning direction to partially overlap the consecutive laser induced lines to create LIPSS with periodicities of 620 nm.

2.3. Characterization methods

The surface morphology of laser ablated Ti surface was analyzed by a field-emission scanning electron microscope (JEOL JSM-7500F) with an accelerating voltage of 2.00 kV. Sample images were acquired at magnifications of x2000 and x7500. The SEM image was processed using the ImageJ software (National Institute of Health) [32] and the spatial periodicity of the laser ablated Ti sample was given using the peak-to-peak measurements. The surface roughness was measured with the Park NX10 AFM system in non-contact mode, scanning over a 5×5 μm^2 area. The AFM image was processed using the XEI software package. The chemical states and relative abundance of the elements on the surface of the

laser ablated samples were examined by XPS (Kratos Axis Ultra DLD) using a mono Al Kα (1486.7 eV) radiation source at 14 kV and 140 W. Fitting of the core-level spectra was performed in CasaXPS v.2.3.18PR1.0, Casa software Ltd., using Gaussian-Lorentzian curves after a Shirley background was subtracted from the data [33]. All XPS spectra are referenced to the adventitious hydrocarbon C1s peak at binding energy of 284.8 eV. A VCA Optima Surface Analysis System (AST Products) was used to measure the static contact angle (CA) of the laser modified samples using the sessile drop technique after automatically dispensing 2 μL deionized water from a microsyringe. The SA was measured with a tilting angle instrument equipped with a camera at room temperature by dispensing 10 μL deionized water droplet from a microsyringe. The value of SA was an average of three measurements obtained on the sample. The laser textured samples were stored under ambient conditions for different periods before performing the water contact measurements.

3. Results and discussion

3.1. Femtosecond laser structured surfaces

The SEM images of the patterns generated on Ti surface with linearly polarized femtosecond laser are presented in Fig. 1. It can be seen from the SEM images shown in Fig. 1 that uniform LIPSS with consistent periodicity over large area has been generated. The average spatial periodicity of LIPSS is 620±12 nm. AFM measurement of a 5x5 μm^2 scan area is used to gain insight about the surface roughness of LIPSS, as shown in Fig. 2. An average surface roughness of 138 ±10 nm is obtained. The periodicity and surface roughness are given as mean ± standard deviation (SD).

3.2. Wettability transition

The surface wettability of the laser textured Ti samples was measured using the sessile drop technique. For each sample, WCA measurements at three different locations were measured and the result is given as the mean ± SD. The samples were stored under ambient conditions for the different periods before the water contact measurements was carried out. The evolution of the contact angle with time for laser textured Ti samples is represented in

Fig. 3. Immediately after the laser treatment, the surface showed superhydrophilic behavior with the water droplet completely wetting the surface. The average WCA of laser textured Ti surfaces increased sharply until day 7, with the sample displaying hydrophobic behavior after 4 days, eventually reaching superhydrophobicity after aging for a year with water droplet not sticking to the surface (WCA=153^{o} ± 2.3^{o}). The representative images of the droplet on the laser ablated Ti surface as a function of time are also shown in Fig. 3. Water droplet (10 μL) rolled off the superhydrophobic surface (SA=5^{o} ± 0.5^{o}) instantaneously due to its water-repellent ability, as shown in supplementary video.

3.3. Surface chemical analysis

The chemical states and relative abundance of the elements in the surface of the fs laser textured Ti samples stored under ambient conditions at different time points after laser treatment were investigated by XPS. The survey spectra of the fresh laser ablated Ti surface, along with samples aged for periods of 45 days and a year are presented in Fig. 4. These spectra reveal that the dominant peaks presented on all these surfaces are the C1s peak, Ti2p peak and O1s peak at binding energies of 284 eV, 458 eV and 531 eV, respectively. The C1s peak presented in all the XPS survey spectra in Fig. 4 is attributed to the presence of adsorbed organic compounds from air onto the surface due to surface contamination. The relative amounts of the adsorbed carbon present on the laser treated surfaces were determined from the XPS survey spectra taken at each time point, as shown in Fig.4. The carbon content on the fresh laser ablated Ti surface, and aged surfaces for periods of 45 days and a year was 22%, 23%, and 26%, respectively.

To obtain more insights into surface polarity, high resolution spectra of the C1s region for the fresh laser ablated Ti surface, samples aged for periods of 45 days, and a year under ambient conditions, are depicted in Fig. 5. The C1s region was deconvoluted into four sub-peaks at binding energies of 284.8 eV, 286.3 eV, 287.8 eV and 288.8 eV assigned to the functional groups hydrocarbon chains (C-C(H)), alcohols/ether (C-O), aldehydes/ketones (C=O) and carboxyl/ester (O-C=O), respectively [34]. The functional group C-C(H) is considered nonpolar and contributes to the hydrophobic property, and the other three functional groups are highly polar contributing to the hydrophilic property [31]. Therefore, the relative concentration of C-C(H) bond on the surface can be taken as an indicator to

probe the nature of the surface wettability. The relative concentration of C-C(H) concentration on the fresh laser ablated Ti surface, samples aged for periods of 45 days and a year stored under ambient conditions, are 79.46%, 78.52% and 80.75%, respectively. The results showed slight change in C-C(H) concentration on the surfaces, indicating that there are other factors contributing to the observed extreme wettability transition.

The high resolution spectra of the Ti2p region of the fresh laser ablated Ti surface, samples aged for periods of 45 days and a year under ambient conditions are shown in Fig. 6. As depicted in Fig. 6, the Ti2p region was deconvoluted into two Ti2p spin-orbital doublets, one at binding energies of 458.5 eV and 464.3 eV, assigned to the Ti $2p_{3/2}$ and Ti $2p_{1/2}$ peaks of Ti^{4+} in TiO_2, and the other at binding energies of 457.1 eV and 462.9 eV assigned to the Ti $2p_{3/2}$ and Ti $2p_{1/2}$ peaks of Ti^{3+} in Ti_2O_3, respectively. In addition, Ti $2p_{3/2}$ peak at 455.3 eV was attributed to Ti^{2+} in TiO. The concentrations of Ti^{2+}, Ti^{3+}, and Ti^{4+} are presented in Fig. 7. The results showed that the fresh laser textured surface has the highest concentration of Ti^{3+} with 11.32%, and the lowest concentration of Ti^{4+} with 87.15%. After aging the samples for 45 days and a year, the concentrations of Ti^{3+} declined to 6.84% and 3.90%, respectively and the concentrations of Ti^{4+} has risen to 91.70% and 95.53%, respectively. In addition, there is negligible contribution from the Ti^{2+} sub-oxide to the laser treated surface. Titanium sub-oxides (Ti_2O_3 and TiO) are eventually transformed to the most thermodynamically stable oxide, TiO_2, over time [35]. The observed trends of Ti^{3+} and Ti^{4+} of these surfaces showed a one-to-one correlation with their corresponding WCAs. The surfaces with lower WCA contained higher amount of Ti^{3+} and the ones with higher WCA contained higher amount of Ti^{4+}. Since there was no change in the surface morphology during the ageing under ambient conditions, the surface chemical composition modification is inferred to be the main reason for the observed gradual wettability transition process, which will be discussed in the next section.

3.4. Mechanism of wettability evolution

Recent research on surface wetting states over the past decades have reported a one-to-one correlation between surface polarity, water molecule orientation at the interface, and wettability. The surface polarity plays a significant role in determining the wettability. Generally, a surface with higher polarity has a higher affinity for water molecules and it is a

highly hydrophilic surface whereas a surface whose interaction with water is predominantely nonpolar is considered hydrophobic [36, 37]. The electronic structure of Ti_2O_3 has a large number of polar sites originating from coordinatively unsaturated Ti and oxygen atoms acting as Lewis acid and base pairs, respectively. The Ti^{3+} at the surface are electron-deficient with seven electrons in their outer orbital, available to accept electron from water oxygen, resulting in hydrophilic hydration structure and hence hydrophilicity, as sketched schematically in Fig. 8a. An explanation for the hydrophobicity of TiO_2 is based on its unique electronic structure. The empty 3d orbitals of Ti atoms in the TiO_2 surface are shielded from interactions with the surrounding environment by the full octet of electrons in the $3s^2p^6$ outer shell orbitals. As a result of the shielding effect, the water affinity of TiO_2 is significantly decreased. Thus, the interfacial water molecules cannot sustain their hydrogen-bonding network and reorient such that only hydrogen bonds between water hydrogen and lattice oxygen can be formed, which is pointing towards the surface leading to a hydrophobic hydration structure, as shown in Fig. 8b [38]. As demonstrated, the unique electronic structure of the TiO_2 and Ti_2O_3 plays a crucial role in the wettability transition of titanium oxide on the laser ablated Ti surface. Previous study reported that aging of oxide surface in air resulted in the adsorption of organic species on the surface [31]. Their result inferred that the accumulation of organic adsorbates on the laser treated surface over time had contributed to a more nonpolar surface and thus leading to wettability transition process to hydrophobicity. In this work, the concentration of carbon C-C(H) was measured using high resolution XPS and the results showed slight change in C-C(H) concentration on the surfaces.

The laser induced submicron structures is another important factor in the observed superhydrophilicity and superhydrophobicity in literature. The two theories to describe the behavior of water droplet on a rough surface are Wenzel [14] and Cassie-Baxter [15]. Immediately after laser ablation, the Ti surface had a higher concentration of Ti2O3 which makes the surface hydrophilic. The water droplet penetrates into the valleys of the LIPSS and completely wets the surface, which can be modeled by Wenzel state. According to the Wenzel theory [14], the increase in surface roughness introduced during the laser processing has an amplification effect on the wettability of the laser ablated surface, suggesting that increasing the surface roughness amplifies the surface inherent wetting behavior, making the

hydrophilic surfaces more hydrophilic. Therefore, the laser induced sub-microstructures amplify the hydrophilicity of the fresh ablated surface resulting in a superhydrophilic surface. After being stored in ambient conditions for a certain period, the concentration of Ti_2O_3 declined and that of TiO_2 increased, turning the laser ablated surface to hydrophobic. In this case, the water droplet cannot penetrate the valleys of the LIPSS due to the formation of a solid-air composite surface, which can be modeled by Cassie-Baxter theory [15]. Here, the laser ablated surface has an amplification effect on hydrophobicity, making the surface superhydrophobic.

4. Conclusions

In this study, the mechanism underlying the wettability transition of the fs laser generated submicron LIPSS on Ti samples from superhydrophilicity right after laser micromachining to superhydrophobicity after aging for a year under ambient conditions from a perspective of detailed XPS analyses of the surface chemical composition of these surfaces at different time points was systematically assessed. The results revealed that the unique electronic structure of Ti_2O_3 and TiO_2 resulting in hydrophilic and hydrophobic hydration structures, respectively, plays a significant role in the wetting transition. According to Wenzel and Cassie-Baxter theories, the increase of surface roughness on Ti surfaces by LIPSS had an amplification effect on both fresh superhydrophilicity and aged superhydrophobicity. This study can further benefit researchers and industries to control the surface wetting behavior for use in biomedical, aeronautical, and industrial applications.

Acknowledgements

We would like to acknowledge Dr. Alexander Mommers and Dr. Yun Liu at the Center for Catalysis Research and Innovation (CCRI), University of Ottawa, for their help with measurement of XPS data and SEM imaging. The AFM imaging was carried out at the Centre for Research in Photonics and the water contact measurements were obtained at the Chemical Engineering Department, University of Ottawa.

Conflicts of Interest

The authors declare no conflict of interest.

References

[1] C. Gao, N. Qua, Electrolysis-assisted recovery of superhydrophilicity from superhydrophobized surfaces, Surf. Coat. Tech. 372 (2019) 343–352.

[2] X. Zhou, S. Yu, S. Guan, Z. Lv, E. Liu, Y. Zhao, Fabrication and characterization of superhydrophobic TiO2 nanotube coating by a facile anodic oxidation approach, Surf. Coat. Tech. 354 (2018) 83–91.

[3] J. Lua, T. Huanga, Z. Liua, X. Zhanga, R. Xiao, Long-term wettability of titanium surfaces by combined femtosecond laser micro/nano structuring and chemical treatments, Appl. Surf. Sci. 459 (2018) 257–262.

[4] X. Xiao, W. Xie, Z. Ye, Preparation of corrosion-resisting superhydrophobic surface on aluminium substrate, Surf. Eng. 35 (2019) 411–417.

[5] M. Sheffer, A. Groysman, and D. Mandler, Electrodeposition of sol–gel films on Al for corrosion protection, Corros. Sci. 45 (2003), 2893–2904.

[6] I. Milošev, T. Kosec, and M. Bele, The formation of hydrophobic and corrosion resistant surfaces on copper and bronze by treatment in myristic acid, J. Appl. Electrochem. 40 (2010), 1317–1323.

[7] W. Xu, H. Liu, S. Lu, J. Xi, and Y. Wang, Fabrication of Superhydrophobic Surfaces with Hierarchical Structure through a Solution-Immersion Process on Copper and Galvanized Iron Substrates, Langmuir 24 (2008), 10895–10900.

[8] 1. C. R. Crick and I. P. Parkin, A single step route to superhydrophobic surfaces through aerosol assisted deposition of rough polymer surfaces: duplicating the lotus effect, J. Mater. Chem. (2009) 19, 1074–1076.

[9] A. Otten and S. Herminghaus, How Plants Keep Dry: A Physicist's Point of View, Langmuir (2004) 20, 2405–2408.

[10] P. Eberle, M. K. Tiwari, T. Maitra, and D. Poulikakos, Rational nanostructuring of surfaces for extraordinary icephobicity, Nanoscale 6 (2014), 4874–4881.

[11] J. Lv, Y. Song, L. Jiang, and J. Wang, Bio-Inspired Strategies for Anti-Icing, ACS Nano 8 (2014), 3152–3169.

[12] J. Drelich, E. Chibowski, D. D. Meng, K. Terpilowski, Hydrophilic and Superhydrophilic Surfaces and Materials. Soft Matter 7 (2011), 9804–9828.

[13] C.R. Crick, S. Ismail, J. Pratten, I.P. Parkin, An investigation into bacterial attachment to an elastomeric superhydrophobic surface prepared via aerosol assisted deposition, Thin Solid Films 519 (2011) 3722–3727.

[14] R. N. Wenzel, Resistance of solid surfaces to wetting by water, Ind. Eng. Chem. 28 (1936), 988–994.

[15] A. B. D. Cassie and S. Baxter, Wettability of porous surfaces, Trans. Faraday Soc. 40 (1944) 546–551.

[16] Y. W. Choi, S. Lee, D. Sohn, Preparation of a superhydrophobic film with UV imprinting technology, Macromol Res 17 (2009) 821–824.

[17] K. Teshimaa, H. Sugimurab, Y. Inouec, O. Takaic, A. Takano, Transparent Ultra Water-Repellent Poly(ethylene terephthalate) Substrates Fabricated by Oxygen plasma Treatment and Subsequent Hydrophobic Coating. Appl. Surf. Sci. 244 (2005), 619–622.

[18] J-H. Kim, A. Mirzaei, H. W. Kim, S. S. Kim, Facile fabrication of superhydrophobic surfaces from austenitic stainless steel (AISI 304) by chemical etching, Facile fabrication of superhydrophobic surfaces from austenitic stainless steel (AISI 304) by chemical etching, Appl. Surf. Sci. 439 (2018), 598–604.

[19] Y. Liu, S.Y. Li, Y.M. Wang, H.Y. Wang, K. Gao, Z.W. Han, L.Q. Ren, Superhydrophobic and superoleophobic surface by electrodeposition on magnesium alloy substrate: Wettability and corrosion inhibition, J. Colloid.Interf. Sci. 478 (2016) 164–171.

[20] S.A. Kamal, R. Ritikos, S.A. Rahman, Wetting behavior of carbon nitride nanostructures grown by plasma enhanced chemical vapor deposition technique, Appl. Surf. Sci. 328 (2015) 146–153.

[21] A. Y. Vorobyev, C. Guo, Effects of nanostructure-covered femtosecond laser- induced periodic surface structures on optical absorptance of metals, Appl. Phys. A 86 (2007) 321-324.

[22] B. Kumar, R. K. Soni, Submicometre periodic surface structures in InP induced by nanosecond UV laser pulses, J. Phys. D: Appl. Phys. 41 (2008) 155303.

[23] S. Baudach, J. Bonse , W. Kautek, Ablation experiments on polyimide with femtosecond laser pulses, Appl. Phys. A 69 (1999) S395-S398.

[24] J. E. Sipe, J. Young, J. Preston, H. van Driel, Laser-induced periodic surface structure. I. Theory, Phys. Rev. B 27 (1983) 1141-1154.

[25] M. Huang, F. Zhao, Y. Cheng, N. Xu, Z. Xu, Origin of Laser-Induced Near-Subwavelength Ripples: Interference between Surface Plasmons and Incident Laser, ACS Nano (2009) 4062-4070.

[26] Y-C Lin, H-M Chen, Y-C Chen, The effect of different methods to add nitrogen to titanium alloys on the properties of titanium nitride clad layers, Mater. Des. 54 (2014) 222–229.

[27] C. Veiga1, J.P. Davim, A.J.R. Loureiro, Properties and applications of titanium alloys: a brief review, Properties and applications of titanium alloys: a brief review, Rev. Adv. Mater. Sci 32 (2012) 14–34.

[28] Y. Tamada, Y. Ikada, Effect of Preadsorbed Proteins on Cell Adhesion to Polymer Surfaces, J. Colloid Interface Sci. 155 (1993) 334–339.

[29] G. Balasundarama, T. J. Webster, A perspective on nanophase materials for orthopedic implant applications, J. Mater. Chem. 16 (2006) 3737–3745.

[30] A. M. Kietzig, S. G. Hatzikiriakos, P. Englezos, Patterned Superhydrophobic Metallic Surfaces, Langmuir 25 (2009) 4821–4827.

[31] J. Long, M. Zhong, P. Fan, D. Gong, H. Zhang, Wettability conversion of ultrafast laser structured copper surface, J. Laser Appl. 27 (2015) S29107.

[32] Rasband, W.S., ImageJ, U. S. National Institutes of Health, Bethesda, Maryland, USA, https://imagej.nih.gov/ij/, 1997-2018.

[33] C.D. Wagner, A.V. Naumkin, A. Kraut-Vass, J.W. Allison, C.J. Powell, J.R. Rumble, Jr., NIST Standard Reference Database 20, Version 3.4 (web version) (http://srdata.nist.gov/xps/).

[34] G. Beamson, D. Briggs, High-resolution XPS of Organic Polymers the Scienta ESCA300 Database, John Wiley and Sons, Toronto, 1992.

[35] M. P. Neupane, I. S. Park, S. J. Lee, K. A. Kim, M. H. Lee, T. S. Bae, Study of Anodic Oxide Films of Titanium Fabricated by Voltammetric Technique in Phosphate Buffer Media, Int. J. Electrochem. Sci. 4 (2009) 197 – 207.

[36] N. Giovambattista, P. G. Debenedetti, Peter J. Rossky, Effect of Surface Polarity on Water Contact Angle and Interfacial Hydration Structure, J. Phys. Chem. B 111 (2007) 9581–9587.

[37] G. Azimi, R. Dhiman, H. M. Kwon, A. T. Paxson, K. K. Varanasi, Hydrophobicity of rare-earth oxide ceramics, Nature Mater. 12 (2013) 315–320.

[38] J. Y. Zheng, S. H. Bao, Y. Guo, P. Jin, Natural Hydrophobicity and Reversible Wettability Conversion of Flat Anatase TiO2 Thin Film, ACS Appl. Mater. Interfaces 6 (2014) 1351–1355.

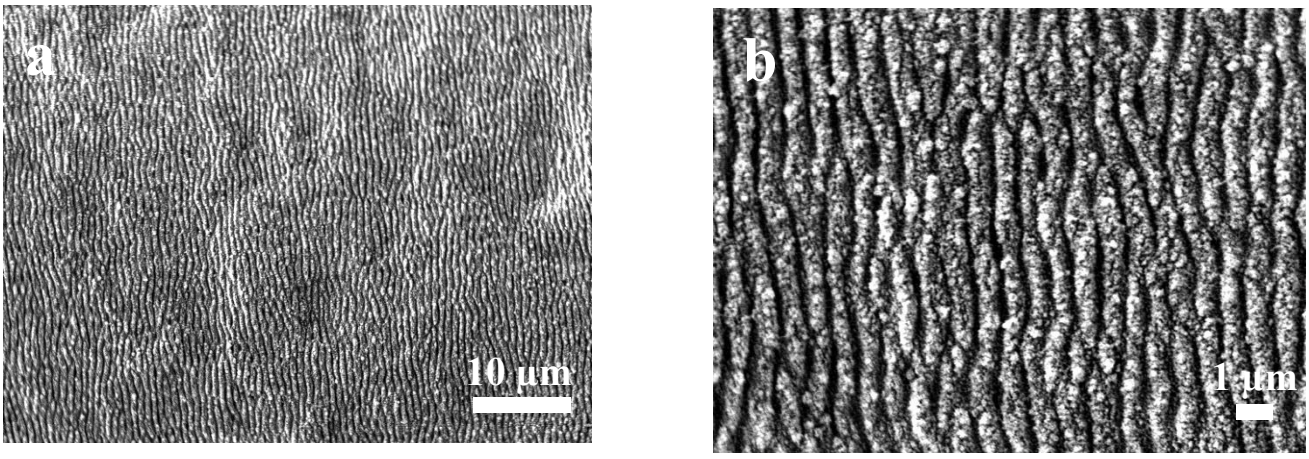

Figure 1: SEM images of the LIPSS on Ti surface with spatial period of 620 nm acquired at (a) lower and (b) higher magnifications.

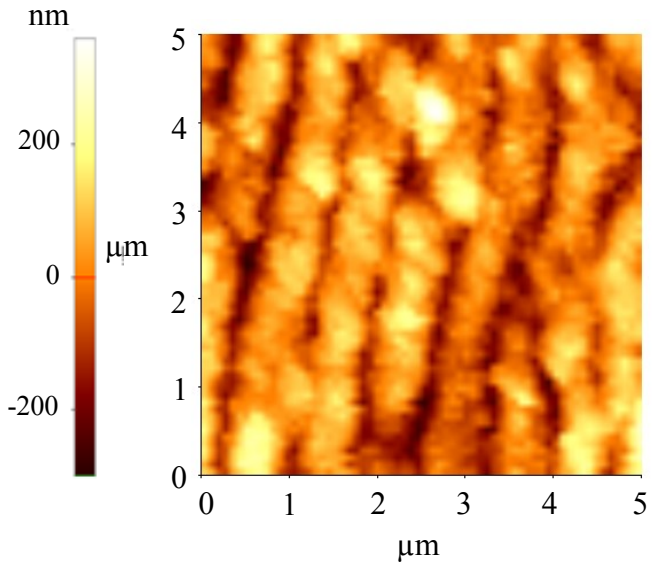

(a)

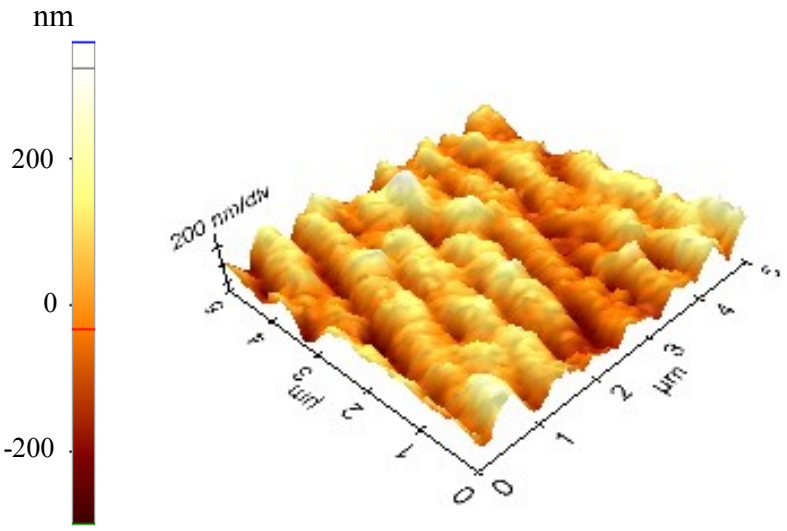

(b)

Figure 2: The (a) 2D and (b) 3D AFM images (scan area of 5x5 µm^2) of the LIPSS with average roughness of 138 nm.

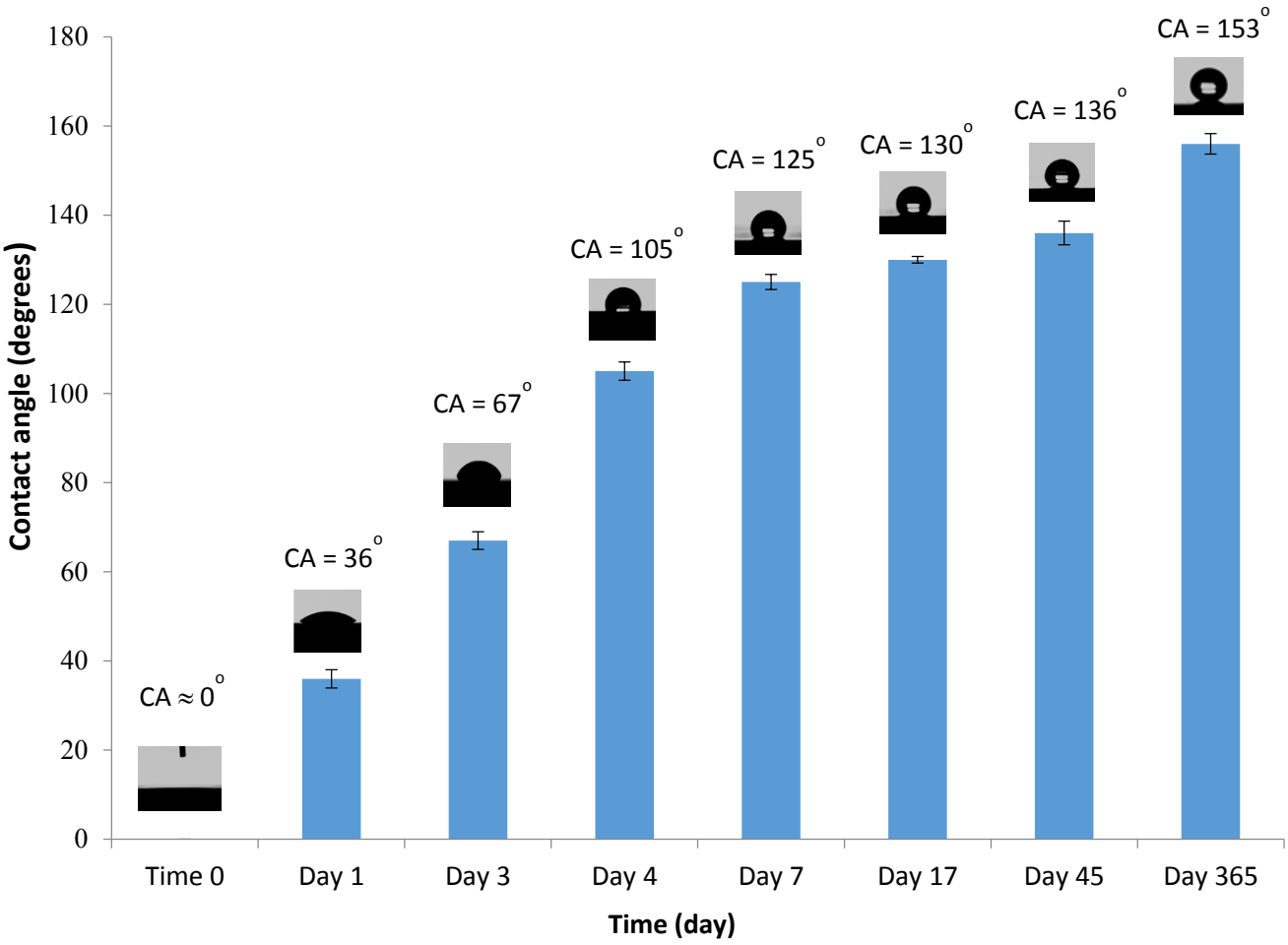

Figure 3: Average water contact angle evolution over 45 days for the laser ablated Ti samples stored under ambient conditions starting right after laser irradiation (t<30mins). The WCA of these samples measured using the sessile drop technique using 2µl deionized water as probe liquid. For each sample, WCA of three different locations were measured and the results are given as the mean ± SD. The representative images of the droplet on the laser ablated Ti surfaces at different time points are also shown.

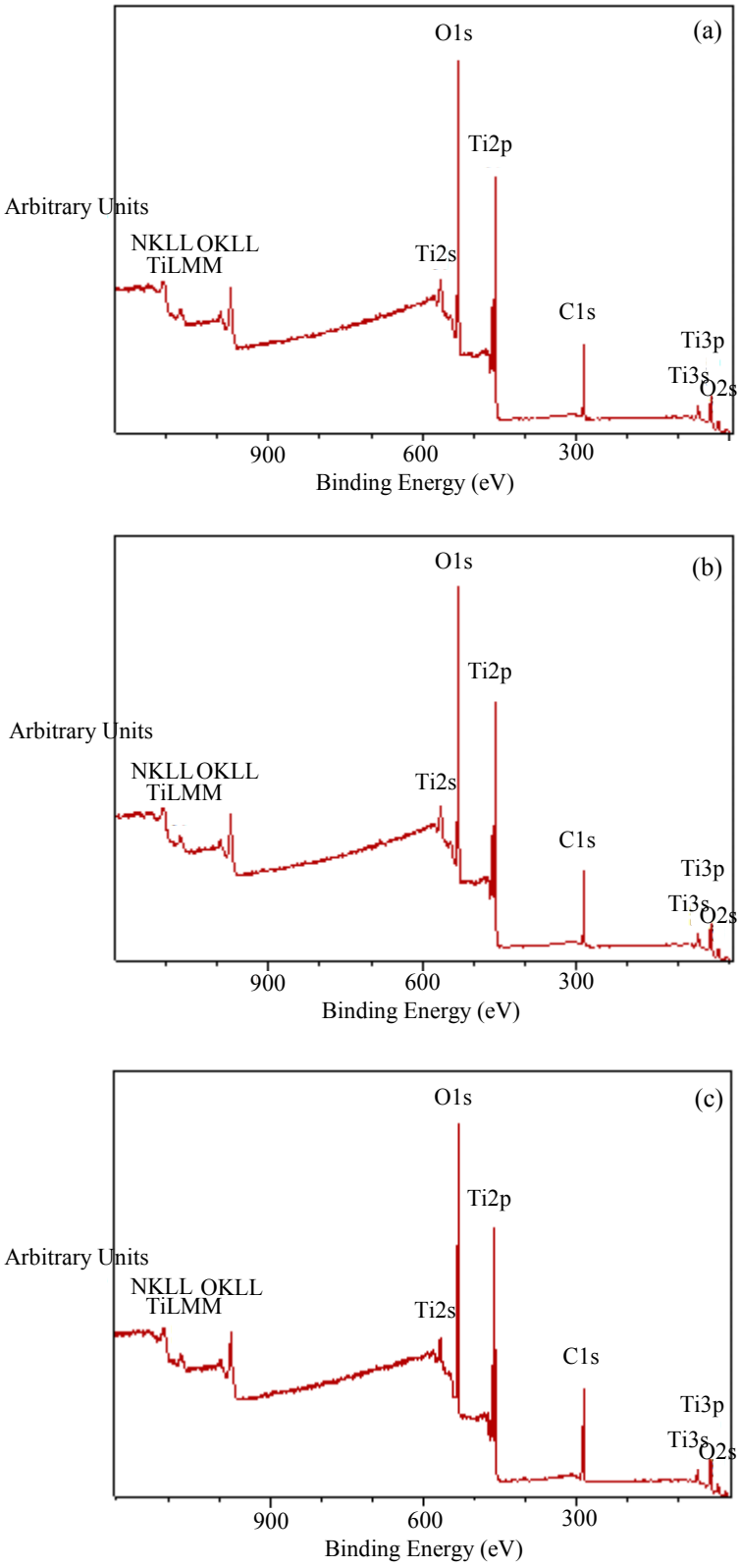

Figure 4: XPS survey spectra of (a) fresh laser ablated Ti sample, (b) after 45 days of aging and (c) a year of aging under ambient conditions.

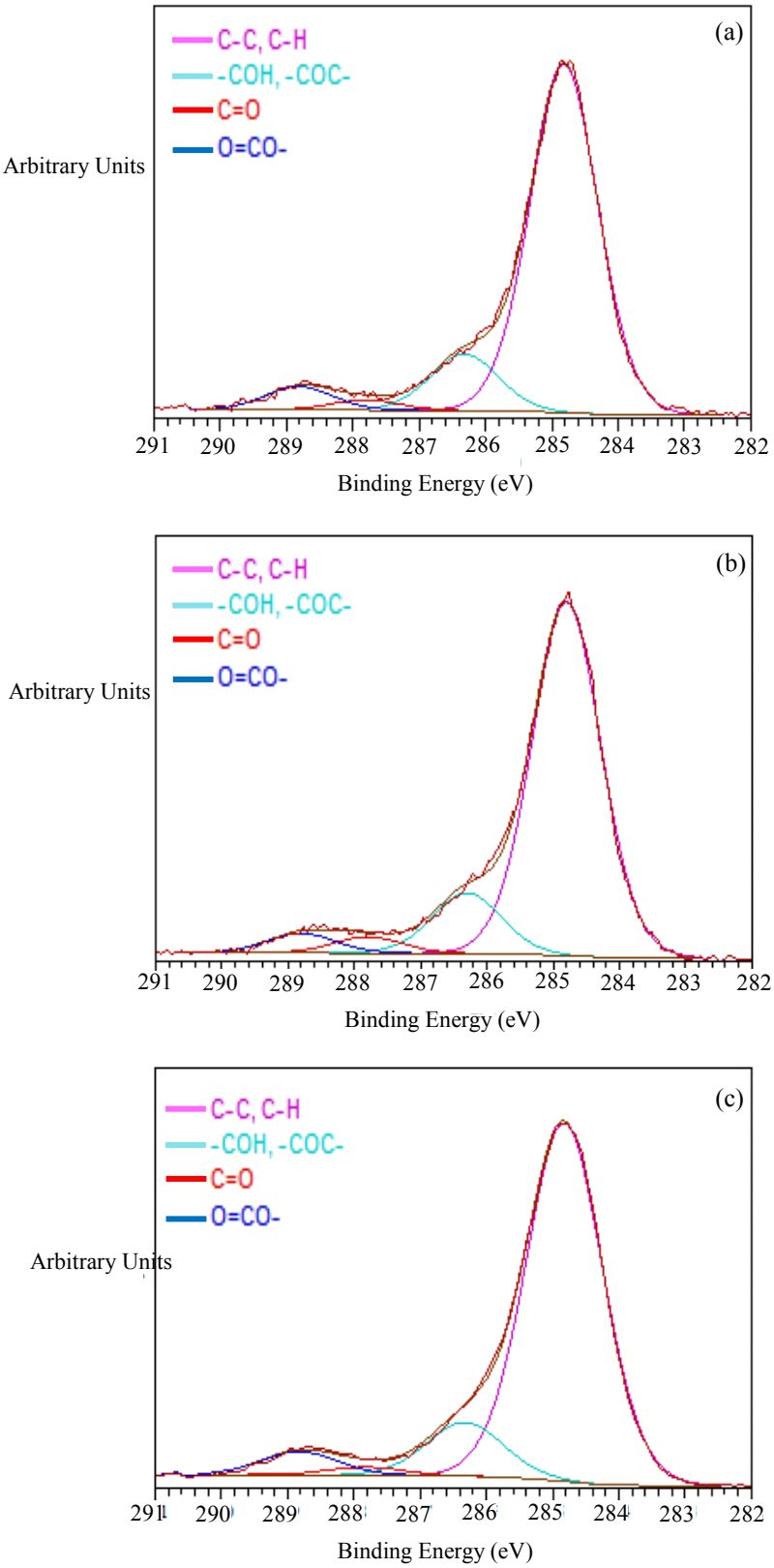

Figure 5: High resolution XPS spectra of the C 1s regions for (a) fresh laser ablated Ti sample, (b) after 45 days of aging and (c) a year of aging under ambient conditions.

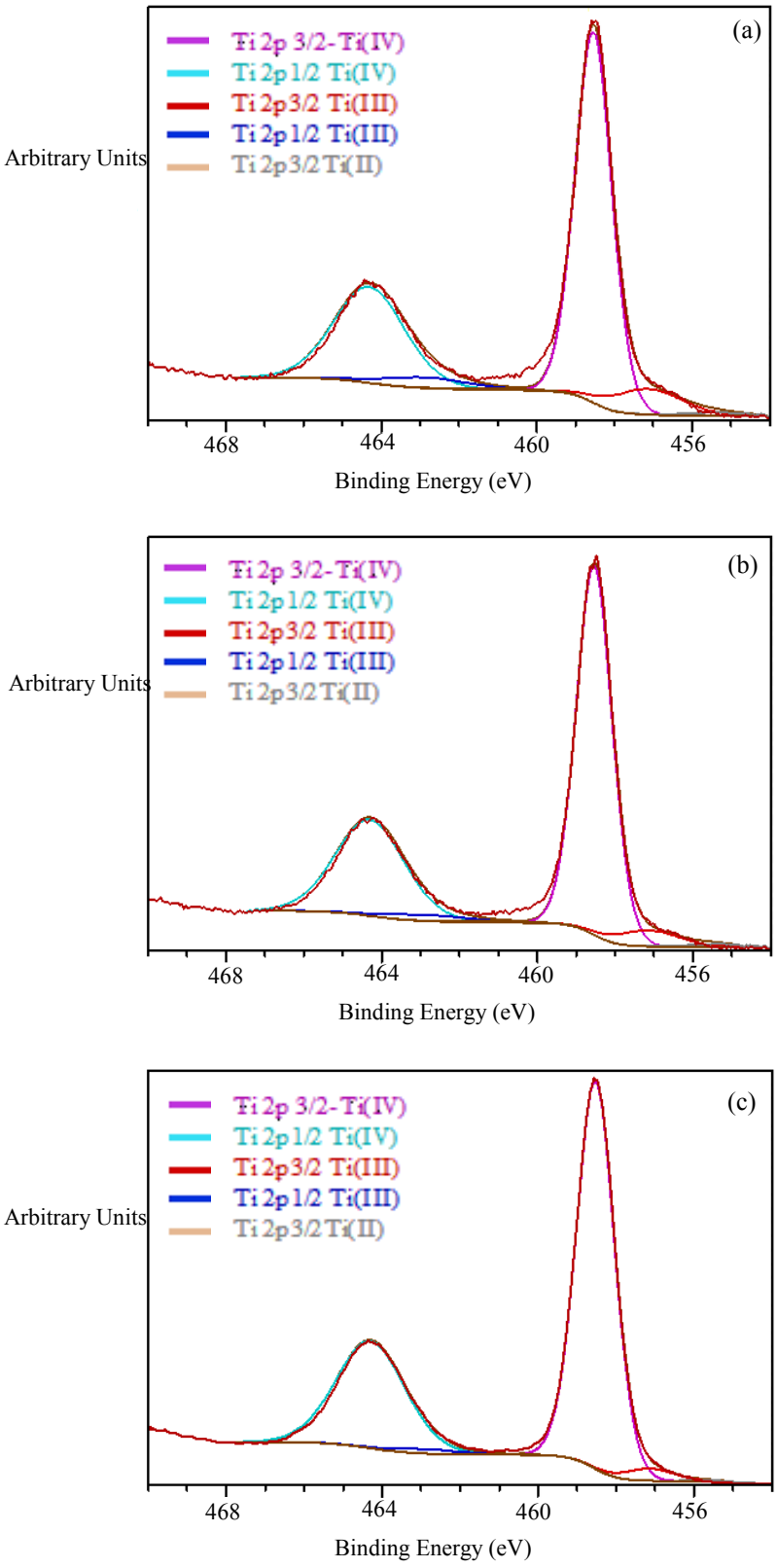

Figure 6: High resolution XPS spectra of Ti2p regions for (a) fresh laser ablated Ti sample, (b) after 45 days of aging and (c) a year of aging under ambient conditions.

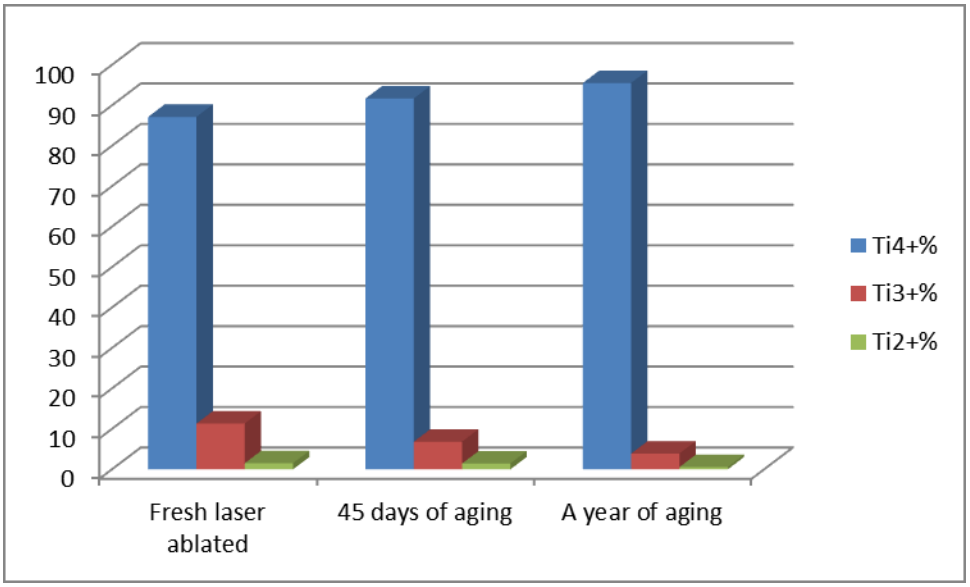

Fig.7. Concentrations of Ti^{4+}, Ti^{3+} and Ti^{2+} for (a) fresh laser ablated Ti sample, (b) after 45 days of aging and (c) a year of aging under ambient conditions.

(a)

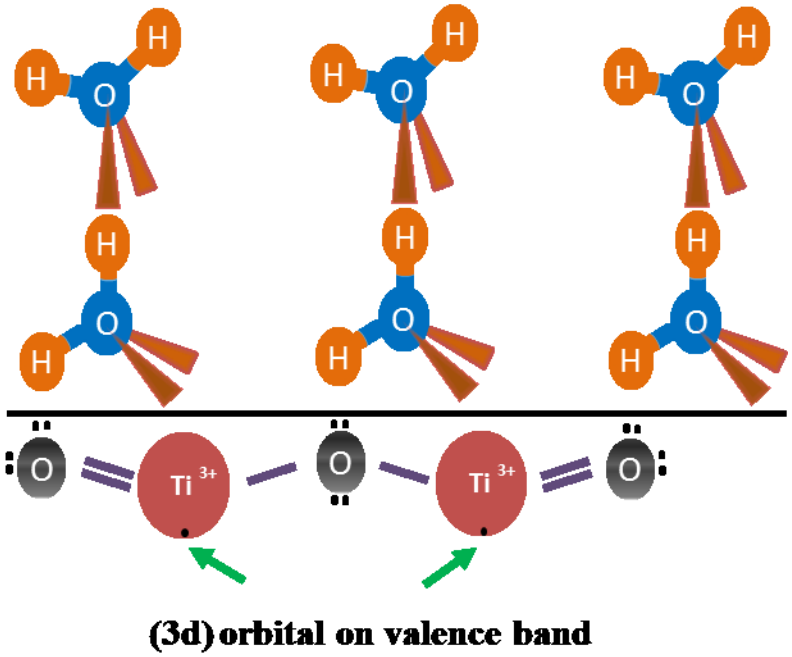

(b)

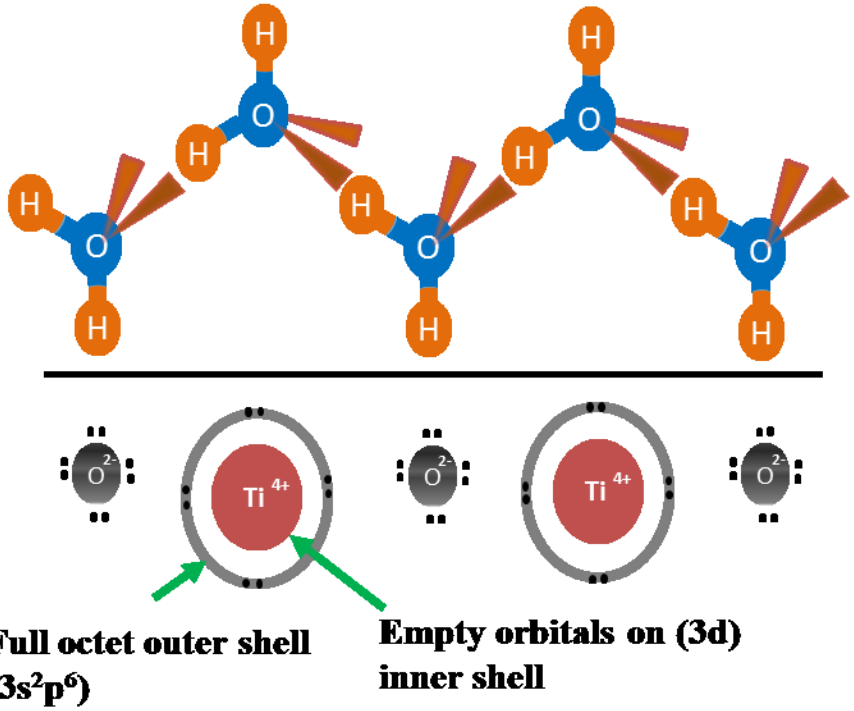

Figure 8: Schematic of the orientation of water molecules next to the (a) hydrophilic surface and (b) hydrophobic surface.

Chapter 5

Conclusions and Suggestions for Future Work

On account of decades of research and development in the field of biomedical technology, innovative orthopedic and dental implants have been produced, improving the quality of life and longevity of patients. Femtosecond laser surface structuring has emerged as a simple, high resolution, fast, controllable, reproducible, contactless, and single step processing technique, providing implants with multiscale surface texturing varying from micro to nanoscale and simultaneously altering their surface chemistry to potentially improve the performance and longevity of next of generation of orthopedic and dental implants.

In this thesis, uniform, reproducible submicron FLIPSS on Ti surfaces with consistent spatial periodicities of 300 nm, 620 nm, and 760 nm, along with consistent roughness and oxide thickness over large area was generated as assessed by SEM, AFM, EELS, and AES. The laser micromachining in air resulted in uniform, stable and thicker oxide layer on all the laser textured surfaces as compared to the control surface, as measured from AES and EELS.

The *in vitro* bioactivity assessments of oasteosarcoma Saos-2 cells on the generated submicron FLIPSS surfaces with consistent periodicities of 300 nm, 620 nm and 760 nm and control surfaces after 3, 7 and 14 days of cell seeding time demonstrated that the cell metabolism and ALP activity on all the surfaces increased in magnitude with cell seeding time, showing laser textured surfaces are not cytotoxic and do not down-regulate cell proliferation. The control surfaces showed a statistically significant ($P < 0.05$) decrease in ALP activity from 7 to 14 days with no corresponding decrease in cell metabolism however this trend was not observed for the laser textured surfaces. The laser textured surface with periodicity of 620 nm outperformed the 300 nm and 760 nm surfaces in cell metabolism and ALP activity at all time points and notably showed statistically significant ($p < 0.05$) increase in ALP activity compared to the control surface at 14 days. As observed under the SEM, the cells appeared to be perpendicularly aligned to the periodic structures of all the laser textured surfaces and also showed a more elongated shape on these surfaces with the filopodia of the cells appear to be attaching to the peaks of the LIPSS as compared with the control surface.

In addition, the cells on all the laser textured surfaces exhibited a decreased circularity and increased nuclear area factor compared to the control surface.

The surface wettability of the laser textured Ti samples evolved over time from exhibiting superhydrophilic behavior immediately after laser texturing, then the WCAs of these surfaces gradually increased over time until the surface turned superhydrophobic after aging for a year under ambient conditions, as assessed by the sessile drop method. Detailed surface chemical analyses by XPS revealed the unique electronic structure of TiO_2 and Ti_2O_3 resulting in hydrophobic and hydrophilic hydration structures, respectively, which played a crucial role in the observed wettability transition. According to Wenzel and Cassie-Baxter theories, the increase of surface roughness on laser textured titanium surfaces had an amplification effect on both fresh superhydrophilicity and aged superhydrophobicity.

The studies described here have demonstrated the prospect of using submicron FLIPSS as a promising surface modification strategy to potentially manipulate cellular behavior. This research has also resulted in new insight into the mechanism underlying the wettability transition of FLIPSS on titanium between the superhydrophilic and superhydrophobic wetting states under ambient conditions.

The present work demonstrated the capability of reproducibly producing consistent submicron FLIPSS over large area on Ti and simultaneously altering their wettability which could potentially be used as a surface modification technique to improve osseointegration of dental and orthopaedic implants.

Some of the suggestions for further research work would be to create FLIPSS with biologically inspired nanoscale periodicities using second or third harmonics of 1030 nm laser wavelength to examine the effect of ordered, repetitive nanoscale laser textured surfaces on the cellular behavior. Moreover, the in vivo studies of the FLIPSS are required to examine the quality and rate of osseointegration over longer times.

Bibliography

[1] Orthopedic Implants Market Outlook – 2025 Available at:

https://www.alliedmarketresearch.com/orthopedic-implants-market; 2019.

[2] D. F. Williams. On the nature of biomaterials, Biomaterials 30 (2009) 5897-5909.

[3] M. Geetha, A.K. Singh, R. Asokamani and A. K. Gogia. Ti based biomaterials, the ultimate choice for orthopedic implants-A review, Progress in Materials Science 54 (2009) 397-425.

[4] Global Orthopedics Market to Grow to $66.2 Billion by 2023 GlobalData, Available at: https://www.odtmag.com/contents/view_breaking-news/2018-03-02/global-orthopedics-market-to-grow-to-662-billion-by-2023/48614 published 03.02.18.

[5] Global Dental Implants Market Worth US$6.54 Billion by 2025: Rising Incidence of Periodontal Diseases Stokes Growth, Available at: https://www.prnewswire.com/news-releases/global-dental-implants-market-worth-us654-billion-by-2025-rising-incidence-of-periodontal-diseases-stokes-growth-634246393.html published Jul 13, 2017, 07:30 ET.

[6] A.F. Mavrogenis, R. Dimitriou, J. Parvizi, and G.C. Babis, Biology of implant osseointegration, J Musculoskelet Neuronal Interact 9 (2009) 61-71.

[7] X. Yu, X. Tang, S. V. Gohil, and C. T. Laurencin, Biomaterials for Bone Regenerative Engineering, Adv Healthc Mater. 4 (2015)1268–1285.

[8] L. Le Gu´ehennec, A. Soueidan, P. Layrolle and Y. Amouriq, Surface treatments of titanium dental implants for rapid osseointegration, dental materials 23 (2007) 844-854.

[9] A. Gaggl, G. Schultes, W.D. Muller, and H. Karcher, Scanning electron microscopical analysis of laser-treated titanium implant surfaces-a comparative study, Biomaterials 21 (2000) 1067-1073.

[10] A. Y. Vorobyev, C. Guo, Effects of nanostructure-covered femtosecond laser- induced periodic surface structures on optical absorptance of metals, Appl. Phys. A 86 (2007) 321-324.

[11] X.C. Wang, G.C. Lim, F.L. Ng, W. Liu, and S.J. Chua, Femtosecond pulsed laser-induced periodic surface structures on GaN/sapphire, Appl. Surf. Sci. 252 (2005) 1492–1497.

[12] K. Ozono, M. Obara, A. Usui, and H. Sunakawa, High-speed ablation etching of GaN semiconductor using femtosecond laser, Optics Communications 189 (2001) 103-106.

[13] S. Baudach, J. Bonse , W. Kautek, Ablation experiments on polyimide with femtosecond laser pulses, Appl. Phys. A 69 (1999) S395-S398.

[14] J. E. Sipe, J. Young, J. Preston, H. van Driel, Laser-induced periodic surface structure. I. Theory, Phys. Rev. B 27 (1983) 1141-1154.

[15] M. Huang, F. Zhao, Y. Cheng, N. Xu, Z. Xu, Origin of Laser-Induced Near-Subwavelength Ripples: Interference between Surface Plasmons and Incident Laser, ACS Nano 3 (2009) 4062-4070.

[16] Matej Balažic and Janez Kopač, Machining of Titanium Alloy Ti-6Al-4V for Biomedical Applications, Journal of Mechanical Engineering 56 (2010) 1-5.

[17] G. Balasundarama, T. J. Webster, A perspective on nanophase materials for orthopedic implant applications, J. Mater. Chem. 16 (2006) 3737–3745.

[18] D. F. Williams. Definitions in biomaterials. Amsterdam: Elsevier; 1987.

[19] C. N. Elias, Factors Affecting the Success of Dental Implants, [Internet]. Rijeka: InTech [cited 2014 Apr 22]. Available at: http://www.intechopen.com/books/implant-dentistry-a-rapidly-evolving-prac¬tice/factors-affecting-the-success-of-dental-implants.

[20] G. Richard Holt, Stephen M. Parel, and P.I. Branemark, Osseointegrated Titanium Implants, Facial Plastic Surgery 3 (1986) 113-124.

[21] T. Albrektsson, P. I. Brånemark, H. A. Hansson and I. Lindström, Osseointegrated titanium Implants. Requirements for ensuring a long-lasting, direct bone-to-implant anchorage in man, Acta Orthop Scand. 52 (1981) 155-170.

[22] A. Wennerberg, C. Hallgren, C. Johansson and S. Danelli, A histomorphometric evaluation of screw-shaped implants each prepared with two surface roughnesses, Clinical Oral Implants Research 9 (1998) 11–19.

[23] R. Smeets, B. Stadlinger, F. Schwarz, B. Beck-Broichsitter, O. Jung, C. Precht, F. Kloss, A. Gröbe, M. Heiland, and T. Ebker, Impact of dental implant surface modifications on osseointegration, BioMed Research International (2016) 1-16.

[24] F. Grizon, E. Aguado, G. Hure, M. F. Basle, D. Chappard, Enhanced bone integration of implants with increased surface roughness: a long term study in the sheep, J Dent. 30 (2002)195–203.

[25] A. Barfeie, J. Wilson and J. Rees, Implant Surface Characteristics and their effect on Osseointegration, British Dental Journal 218 (2015) 1-8.

[26] N. N. Pardeshi, C. Zhou, T. W. Randolph, and J. F. Carpenter, Protein nanoparticles promote microparticle formation in intravenous immunoglobulin solutions during freeze-thawing and agitation stresses, J Pharm Sci. 107 (2018) 1852–1857.

[27] X. Wang, Z. Schwartz, R. A. Gittens, A. Cheng, R. Olivares-Navarrete, H. Chen, B. D. Boyan. 2015. Role of integrin α2β1 in mediating osteoblastic differentiation on three-dimensional titanium scaffolds with submicron-scale texture. J Biomed Mater Res A. 103 (2015)1907–1918.

[28] Ann Wennerberg, Tomas Albrektsson, and Jukka Lausmaa, Torque and histomorphometric evaluation of c.p. titanium screws blasted with 25- and 75-pm-sized particles of Al2O3, J. Biomed. Mater. Res. 30 (1996) 251-260.

[29] C. J. Ivanoff, C. Hallgren, G. Widmark, L. Sennerby and A. Wennerberg, Histologic evaluation of the bone integration of TiO_2 blasted and turned titanium micro implants in humans, Clin Oral Implants Res 12 (2001)128–34.

[30] L. Rasmusson, J. Roos and H. Bystedt, A 10-year follow-up study of titanium dioxide-blasted implants. Clin Implant Dent Relat Res 7 (2005) 36–42.

[31] L. Gaviria, J. P. Salcido, T. Guda, J. L. Ong, Current trends in dental implants, 40 (2014) 50-60.

[32] C. N. Elias, Titanium dental implant surfaces, Matéria (Rio J.) 15 (2010) 138–142.

[33] A. Ombelli and N. P. Lang, The diagnosis and treatment of peri-implantitis, Periodontology 17 (1998) 63-76.

[34] Sebastian Bauer, Sebastian Kleber, Patrik Schmuki, TiO_2 nanotubes: Tailoring the geometry in H3PO4/HF electrolytes, Electrochemistry Communications 8 (2006) 1321–1325.

[35] J. J. Norman and T. A. Desai, Methods for fabrication of nanoscale topography for tissue engineering scaffolds, Annals of Biomedical Engineering 34 (2006) 89–101.

[36] K. Sugioka, M. Meunier and A. Piqu´. Laser Precision Microfabrication. Springer, Springer-Verlag Berlin Heidelberg, 2010, 91-120,

[37] A. Carvalhoa, L. Cangueiro, V. Oliveira, R. Vilar, M. H. Fernandes, F. J. Monteiro, Femtosecond laser microstructured Alumina toughened Zirconia: A new strategy to improve osteogenic differentiation of hMSCs, Appl. Surf. Sci. 435 (2018) 1237–1245.

[38] A. Cunha, O. F. Zouani, L. Plawinski, A. M. Botelho do Rego, A. Almeida, R. Vilar, Human mesenchymal stem cell behavior on femtosecond laser-textured Ti-6Al-4V surfaces. Nanomedicine (Lond). 10 (2015) 725–739.

[39] K. M. T. Ahmmed, C. Grambow and A-M Kietzig, Fabrication of Micro/Nano Structures on Metals by Femtosecond Laser Micromachining, Micromachines 5 (2014) 1219-1253.

[40] A. Y. Vorobyev and C. Guo, Direct femtosecond laser surface nano/microstructuring and its applications, Laser Photonics Rev. 7 (2013) 385–407.

[41] E.L. Gurevicha and S.V. Gurevich, Laser Induced Periodic Surface Structures induced by surface plasmons coupled via roughness, Appl. Surf. Sci. 302 (2014)118–123.

[42] P.T. Mannion, J. Magee, E. Coyne, G.M. O'Connor and T.J. Glynn, The effect of damage accumulation behaviour on ablation thresholds and damage morphology in ultrafast laser micro-machining of common metals in air, Appl. Surf. Sci. 233 (2004) 275–287

[43] J. M. Liu, pulsed Gaussian-beam spot sizes, Opt. Lett. 7 (1982) 196-198.

[44] M. Birnbaum, Semiconductor surface damage produced by ruby lasers, J. Appl. Phys. 36 (1965) 3688-3689.

[45] A. Borowiec and H. K. Haugen, Subwavelength ripple formation on the surfaces of compound semiconductors irradiated with femtosecond laser pulses, Appl. Phys. Lett. 82 (2003) 4462–4464.

[46] F. Costache, S. Kouteva-Arguirova and J. Reif, Sub–damage–threshold femtosecond laser ablation from crystalline Si: surface nanostructures and phase transformation, Appl. Phys.A 79 (2004)1429–1432.

[47] J. Bonse, M. Munz, and H. Sturm, Structure formation on the surface of indium phosphide irradiated by femtosecond laser pulses, J. Appl. Phys. 97 (2005) 013538.

[48] A.Y. Vorobyev and C. Guo, Antireflection effect of femtosecond laser-induced periodic surface structures on silicon, Opt. Express 19 (2011) A1031–A1036.

[49] A.Y. Vorobyev and C. Guo, Enhanced absorptance of gold following multipulse femtosecond laser ablation, Phys. Rev. B 72 (2005) 195422.

[50] A.Y. Vorobyev and C. Guo, Femtosecond laser structuring of titanium implants, Appl. Surf. Sci. 253 (2007) 7272–7280.

[51] A.Y. Vorobyev, V. S. Makin, and C. Guo, Periodic ordering of random surface nanostructures induced by femtosecond laser pulses on metals, J. Appl. Phys. 101 (2007) 034903.

[52] J. Wang and C. Guo, Ultrafast dynamics of femtosecond laser-induced periodic surface pattern formation on metals, Appl. Phys. Lett. 87 (2005) 251914.

[53] C. Hnatovsky, J. R. Taylor, P. P. Rajeev, E. Simova, V. R. Bhardwaj, D. M. Rayner, and P. B. Corkum, Pulse duration dependence of femtosecond-laser-fabricated nanogratings in fused silica, Appl. Phys. Lett. 87 (2005) 14104–14106.

[54] M. Rohloff, S. K. Das, S. Höhm, R. Grunwald, A. Rosenfeld, J. Krüger, and J. Bonse, Formation of laser-induced periodic surface structures on fused silica upon multiple cross-polarized double-femtosecond-laser-pulse irradiation sequences, J. Appl. Phys. 110 (2011) 014910.

[55] R. Wagner, J. Gottmann, A. Horn, and E.W. Kreutz, Subwavelength ripple formation induced by tightly focused femtosecond laser radiation, Appl. Surf. Sci. 252 (2006) 8576–8579.

[56] J. Bonse, R. Koter, M. Hartelt, D. Spaltmann, S. Pentzien, S. Hohm, A. Rosenfeld,J. Kruger, Femtosecond laser-induced periodic surface structures on steel and titanium alloy for tribological applications, Appl. Phys. A 117 (2014) 103–110.

[57] M. Zupančič, M. Steinbücher, P. Gregorčič, I. Golobič, Enhanced pool-boilingheat transfer on laser-made hydrophobic/superhydrophilic polydimethylsiloxane-silica patterned surfaces, Appl. Therm. Eng. 91 (2015) 288–297.

[58] A. Pan, A. Dias, M. Gomez-Aranzadi, S. M. Olaizola, and A. Rodriguez, Formation of laser-induced periodic surface structures on niobium by femtosecond laser irradiation, J. Appl. Phys. 115 (2014) 173101.

[59] A. Y. Vorobyev and Chunlei Guo, Femtosecond laser-induced periodic surface structure formation on Tungsten, J. Appl. Phys. 104 (2008) 063523, 2008.

[60] T. K. Hwang and C. Guo, Angular effects of nanostructure-covered femtosecond laser induced, J. Appl. Phys. 108 (2010) 073523.

[61] J. Reif, O. Varlamova, F. Costache, Femtosecond laser induced nanostructure formation: self-organization control parameters, Appl. Phys. A 92 (2008)1019–1024.

[62] O. Varlamova, J. Reif, S. Varlamov, M. Bestehorn, The laser polarization as control parameter in the formation of laser-induced periodic surfaces tructures: comparison of numerical and experimental results, Appl. Surf. Sci. 257 (2011) 5465–5469.

[63] J. Wang and C. Guo, Permanent recording of light helicity on optically inactive metal surfaces, Opt. Lett. 24 (2006) 3641-3643.

[64] Y. Tang, J. Yang, B. Zhao, M. Wang and X. Zhu, Control of periodic ripples on metals by femtosecond laser ellipticity, Opt. Express 23 (2012) 25826-25833.

[65] O. Varlamova, F. Costache, M. Ratzke, and J. Reif, Control parameters in pattern formation upon femtosecond laser ablation, Appl. Surf. Sci. 253 (2007) 7932–7936.

[66] F. He, Y. Liao, J. Lin, J. Song, L. Qiao, Y. Cheng and K. Sugioka, Femtosecond Laser Fabrication of Monolithically Integrated Microfluidic Sensors in Glass, Sensors 14 (2014) 19402-19440.

[67] Y. Tamada, Y. Ikada, Effect of Preadsorbed Proteins on Cell Adhesion to Polymer Surfaces, J. Colloid Interface Sci. 155 (1993) 334–339.

[68] G. Balasundarama, T. J. Webster, A perspective on nanophase materials for orthopedic implant applications, J. Mater. Chem. 16 (2006) 3737–3745.

[69] D.Y. Kwok and A.W. Neumann, Contact angle measurement and contact angle interpretation, Adv. Colloid Interface Sci. 81(1999) 167-249.

[70] E. Fadeeva and B. Chichkov, Biomimetic Liquid-Repellent Surfaces by Ultrafast Laser Processing, Appl. Sci. 8 (2018) 1424-1446,

[71] T. Young, An essay on the cohesion of fluids, Philos. Trans. Royal Soc. A 95 (1805) 65-87.

[72] K. Seo, M. Kim and D. H. Kim, Re-derivation of Young's Equation, Wenzel Equation, and Cassie-Baxter Equation Based on Energy Minimization, IntechOpen, Available at: https://www.intechopen.com/books/surface-energy/re-derivation-of-young-s-equation-wenzel-equation-and-cassie-baxter-equation-based-on-energy-minimiz.

[73] R.N. Wenzel, Resistance of solid surfaces to wetting by water, Ind. Eng. Chem. 28 (1936) 988–994.

[74] A-M Kietziga, M. N. Mirvakili, S. Kamal, P. Englezos and S. G. Hatzikiriakos, Metallic Substrates: Cassie to Wenzel Wetting Transitions, Journal of Adhesion Science and Technology 25 (2011) 2789–2809.

[75] A. Cassie, S. Baxter, Wettability of porous surfaces. Trans. Faraday Soc. 40 (1944) 546–551.